Article

Structure, function and pharmacology of human itch GPCRs

https://doi.org/10.1038/s41586-021-04126-6

Received: 14 May 2021

Accepted: 8 October 2021

Published online: 17 November 2021

Check for updates

Can Cao[1,11], Hye Jin Kang[1,11], Isha Singh[2], He Chen[3], Chengwei Zhang[3], Wenlei Ye[4], Byron W. Hayes[5], Jing Liu[3], Ryan H. Gumpper[1], Brian J. Bender[2], Samuel T. Slocum[1], Brian E. Krumm[1], Katherine Lansu[1], John D. McCorvy[1,9], Wesley K. Kroeze[1], Justin G. English[1,10], Jeffrey F. DiBerto[1], Reid H. J. Olsen[1], Xi-Ping Huang[1], Shicheng Zhang[1], Yongfeng Liu[1], Kuglae Kim[1], Joel Karpiak[2], Lily Y. Jan[4,6], Soman N. Abraham[5,7], Jian Jin[3], Brian K. Shoichet[2]✉, Jonathan F. Fay[8]✉ & Bryan L. Roth[1]✉

The MRGPRX family of receptors (MRGPRX1–4) is a family of mas-related G-protein-coupled receptors that have evolved relatively recently[1]. Of these, MRGPRX2 and MRGPRX4 are key physiological and pathological mediators of itch and related mast cell-mediated hypersensitivity reactions[2–5]. MRGPRX2 couples to both G_i and G_q in mast cells[6]. Here we describe agonist-stabilized structures of MRGPRX2 coupled to G_{i1} and G_q in ternary complexes with the endogenous peptide cortistatin-14 and with a synthetic agonist probe, respectively, and the development of potent antagonist probes for MRGPRX2. We also describe a specific MRGPRX4 agonist and the structure of this agonist in a complex with MRGPRX4 and G_q. Together, these findings should accelerate the structure-guided discovery of therapeutic agents for pain, itch and mast cell-mediated hypersensitivity.

The sensation of itch (pruritis) can be triggered by many environmental insults, including insect bites, parasites, skin diseases such as eczema, liver and kidney diseases, and hypersensitivity reactions to commonly prescribed medications[7]. Itch has both neuronal[7] and non-neuronal components, with histamine release from mast cells being prominent[8]. Several transmitters have been implicated in sensing and mediating the itch response, including histamine, interleukin and various peptides. Molecular targets involved in itch include G-protein-coupled receptors (GPCRs), cytokine receptors and ion channels[7]. Mas-related GPCRs (MRGPRs) have recently been identified as pruritogenic receptors[4,9].

Structures of MRGPRX2–G protein complexes

MRGPRs are divided into nine major clades: MRGPRA to MRGPRH and MRGPRX. The MRGPRX group of receptors has been identified as being enriched in human sensory neurons[10]. The group comprises four members: MRGPRX1, MRGPRX2, MRGPRX3 and MRGPRX4. MRGPRX4 mediates cholestatic itch[4], whereas MRGPRX2 regulates mast cell degranulation and itch-related hypersensitivity reactions[2,11]. We identified MRGPRX2 and MRGPRX4 as targets for commonly prescribed medications that induce itch and mast cell-mediated hypersensitivity as side effects. These include the anti-diabetic drug nateglinide[12], which acts on MRGPRX4, and several morphinan alkaloids including morphine, codeine and dextromethorphan, which act on MRGPRX2[13]. Using structure-based drug discovery, we also identified a selective MRGPRX2 agonist that can induce degranulation in mast cells[13].

Despite controversy regarding the canonical MRGPRX2 signalling pathways[14], we found that MRGPRX2 effectively coupled to nearly all G-protein families (Extended Data Fig. 1) with robust coupling at both G_q- and G_i-family α-subunits[15]. Accordingly, we determined structures of MRGPRX2 complexed with G_q and G_{i1} using the MRGPRX2-selective small-molecule agonist (*R*)-ZINC-3573[13] and the peptide cortistatin-14 at global resolutions of 2.9 Å, 2.6 Å, 2.45 Å and 2.54 Å, respectively (Fig. 1a–d, Extended Data Figs. 2, 3), using single-particle cryo-electron microscopy (cryo-EM).

The high-resolution maps of MRGPRX2 enabled unambiguous building of its seven transmembrane (TM) domains. Both cortistatin-14 and (*R*)-ZINC-3573 adopt similar conformations in the G_{i1}- or G_q-coupled MRGPRX2 structures (Extended Data Fig. 4a, b, d). The cryo-EM maps showed better ligand densities in the G_q-coupled MRGPRX2 complexes (Extended Data Fig. 2, 3); thus, our structural analysis of ligand poses is mainly focused on G_q-coupled MRGPRX2 complex structures, unless otherwise specified. As recently discussed[16], MRGPRX2 lacks, or contains modified versions of, many of the canonical trigger motifs seen in other family A GPCRs (Extended Data Fig. 5a). These include: (1) the absence of the P–I–F ($P^{5.50}$, $I^{3.40}$, $F^{6.44}$) motif[17]; (2) a semi-conserved DRY motif in TM3 (ERC in MRGPR family receptors); (3) lack of a key TM3 residue for conserved sodium binding; (4) absence of the 'toggle switch' tryptophan ($W^{6.48}$) which is replaced[17] by a glycine ($G^{6.48}$).

[1]Department of Pharmacology, University of North Carolina at Chapel Hill School of Medicine, Chapel Hill, NC, USA. [2]Department of Pharmaceutical Sciences, University of California San Francisco, School of Medicine, San Francisco, CA, USA. [3]Mount Sinai Center for Therapeutics Discovery, Departments of Pharmacological Sciences, Oncological Sciences and Neuroscience, Tisch Cancer Institute, Icahn School of Medicine at Mount Sinai, New York, NY, USA. [4]Department of Physiology, University of California, San Francisco, San Francisco, CA, USA. [5]Department of Pathology, Duke University Medical Center, Durham, NC, USA. [6]Howard Hughes Medical Institute, San Francisco, CA, USA. [7]Program in Emerging Infectious Diseases, Duke–National University of Singapore, Singapore, Singapore. [8]Department of Biochemistry and Biophysics, University of North Carolina at Chapel Hill School of Medicine, Chapel Hill, NC, USA. [9]Present address: Department of Cell Biology, Neurobiology and Anatomy, Medical College of Wisconsin, Milwaukee, WI, USA. [10]Present address: Department of Biochemistry, University of Utah School of Medicine, Salt Lake City, UT, USA. [11]These authors contributed equally: Can Cao, Hye Jin Kang. ✉e-mail: bshoichet@gmail.com; fayj@unc.edu; bryan_roth@med.unc.edu

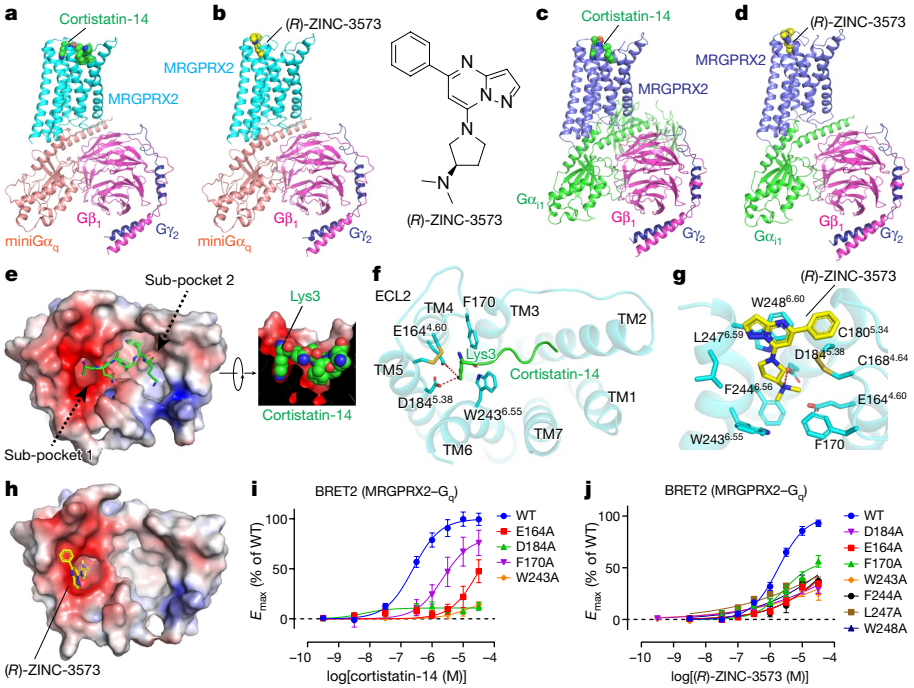

Fig. 1 | Cryo-EM structures of MRGPRX2 complexes. a–**d**, Cartoon representations of MRGPRX2–G_q–cortistatin-14 complex (**a**), MRGPRX2–G_q–(*R*)-ZINC-3573 complex (**b**), MRGPRX2–G_{i1}–cortistatin-14 complex (**c**) and the MRGPRX2–G_{i1}–(*R*)-ZINC-3573 complex (**d**). **e**, Electrostatic surface representation of the MRGPRX2 extracellular pocket calculated using the APBS plugin in PyMOL with cortistatin-14 shown as green sticks. Red, negative (−5 kT e^{-1}); blue, positive (+5 kT e^{-1}). The cross-section image shows the good fit of Lys3 of cortistatin-14 to sub-pocket 1. **f**, Binding pocket of cortistatin-14. Key residues of MRGPRX2 interacting with the Lys3 of corstitatin-14 are shown as sticks. Hydrogen bonds are shown as red dashed lines. **g**, Key residues involved in (*R*)-ZINC-3573 binding in MRGPRX2. Charge interactions are shown as red dashed lines. **h**, Electrostatic surface representation of the MRGPRX2 extracellular pocket with (*R*)-ZINC-3573 shown as yellow sticks. Red, negative (−5 kT e^{-1}); blue, positive (+5 kT e^{-1}). **i**, Alanine substitution of MRGPRX2 residues interacting with the Lys3 of cortistatin-14 reduced cortistatin-14-stimulated G_q activation. Data are mean ± s.e.m. of $n = 3$ biological replicates. **j**, Bioluminescence resonance energy transfer assay 2 (BRET2) validation of the (*R*)-ZINC-3573 binding pocket. Data are mean ± s.e.m. of $n = 3$ biological replicates. E_{max}, maximum effect; WT, wild type.

Consequently, activated MRGPRX2 has several distinctive features in these key motifs. Specifically, residues of TM5 in MRGPRX2 shift downwards by two residues with L194$^{5.48}$, which is in the equivalent position of P$^{5.50}$ in other GPCRs, engaging with the other two P-I-F motif residues L117$^{3.40}$ and F232$^{6.44}$ (Extended Data Fig. 6a). Additionally, the conserved toggle switch W$^{6.48}$ is replaced with G$^{6.48}$ in MRGPRX2 and TM6 of MRGPRX2 is shifted towards TM3 at the extracellular side, which may hinder ligand binding to the typical family A orthosteric pocket (Extended Data Fig. 6b, c). Accordingly, both corstitatin-14 and (*R*)-ZINC-3573 bind to MRGPRX2 at a position that is distant from the conventionally described family A agonist binding site and closer to the extracellular vestibule (Extended Data Fig. 6c). Finally, the conserved disulfide bond between TM3 and extracellular loop 2 (ECL2) found in family A GPCRs is absent in MRGPRX2. Instead, an inter-helix disulfide bond occurs between C168$^{4.64}$ and C180$^{5.34}$ that is predicted to be found in all the human MRGPR family receptors (Fig. 1f, g, Extended Data Fig. 5a, b). Mutagenesis studies suggest this observed TM4–TM5 disulfide bond is essential for the signalling integrity of MRGPRX2 (Extended Data Fig. 5c, d).

Without the restriction introduced by the class A canonical TM3–ECL2 disulfide bond, ECL2 of MRGPRX2 is flipped to the top of TM4 and TM5, resulting in an uncharacteristically wide-open extracellular ligand binding surface (Fig. 1e, f). Calculation of the electrostatic potential surface revealed that the MRGPRX2 pocket is highly negatively charged on one side (sub-pocket 1 formed by TM3–6 and ECL2) and relatively hydrophobic on the other (sub-pocket 2 formed by TM1–3, and TM6 and TM7) (Fig. 1e, h). Cortistatin-14 binds to a shallow pocket in MRGPRX2 near the extracellular loops (Fig. 1e, f, Extended Data Fig. 6c), which reduces its local resolution—although we were able to model several key cortistatin-14 residues on the basis of the cryo-EM map (Extended Data Fig. 3d). The basic residue Lys3 of cortistatin-14 binds in the negatively charged sub-pocket 1 and forms strong charge interactions with D184$^{5.38}$ and E164$^{4.60}$ (Fig. 1e, f). The remaining resolved residues of cortistatin-14 extend over W243$^{6.55}$ and F170^{ECL2} of MRGPRX2 and bind to sub-pocket 2 mainly through hydrophobic interactions (Fig. 1e, f). This charge–hydrophobic binding mode of cortistatin-14 is consistent with previous observations showing that MRGPRX2 binds multiple peptides enriched in positively charged and aromatic residues[18]. A W243A$^{6.55}$ mutation abolished the activity of cortistatin-14 and the F170^{ECL2}A mutation reduced the potency of cortistatin-14 (Fig. 1i, Supplementary Table 1), indicating that these two bridging residues are important in maintaining a proper pocket shape for ligand engagement and receptor activation. Indeed, the diameter of sub-pocket 1 is so small that it allows only one side chain of a residue to fit (Fig. 1e). As the activation of MRGPRX2 appears to be triggered by agonist binding to sub-pocket 1 (Fig. 1h), many basic peptides could potentially activate MRGPRX2, given that a Lys or Arg side chain is able to fit into the acidic sub-pocket 1, almost irrespective of their main-chain conformation. This may explain the observation that MRGPRX2 is promiscuously activated by many basic peptides.

Unlike cortistatin-14, the small molecule agonist (*R*)-ZINC-3573 bound only to the negatively charged sub-pocket 1 (Fig. 1h). The pyrazolo[1,5-a] pyrimidine moiety of (*R*)-ZINC-3573 lies parallel with W248$^{6.60}$ through a π–π interaction, whereas its 5-phenyl moiety extends towards ECL2 and stacks with the C168$^{4.64}$–C180$^{5.34}$ disulfide (Fig. 1g). The *N*-dimethyl moiety of (*R*)-ZINC-3573 is directly inserted into a cavity formed by F170^{ECL2}, W243$^{6.55}$, F244$^{6.56}$, D184$^{5.38}$ and E164$^{4.60}$, where it forms ion pairs with D184$^{5.38}$ and E164$^{4.60}$ (Fig. 1g). Alanine substitutions of D184$^{5.38}$ and

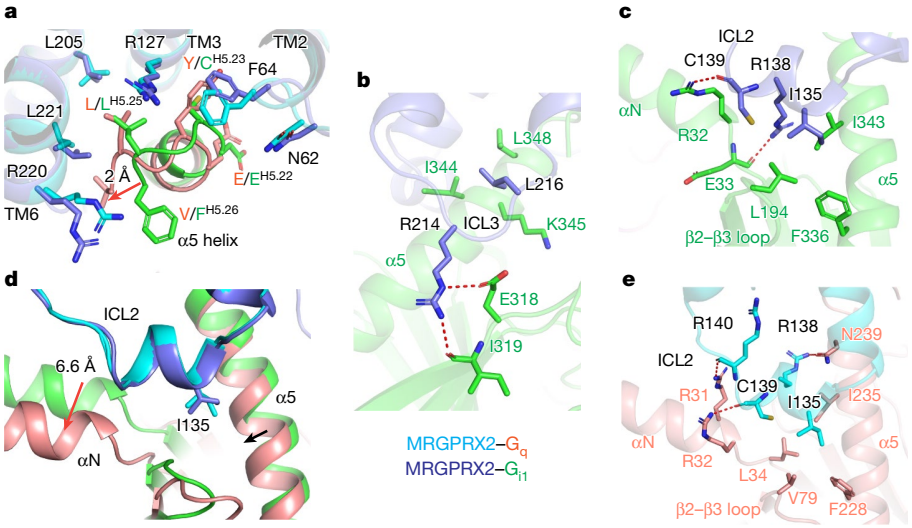

Fig. 2 | G-protein coupling of MRGPRX2. a, The α5-helix of G_q engages the cytoplasmic core of MRGPRX2 in a way distinct from G_{i1}. The relative displacement of G_q with respect to G_{i1} is indicated with an red arrow. The receptor and G_q protein of the MRGPRX2–G_q complex are coloured cyan and red, respectively. The receptor and G_{i1} protein of the MRGPRX2–G_{i1} complex are coloured blue and green, respectively. **b**, **c**, The detailed interactions of MRGPRX2 ICL3 (**b**) and ICL2 (**c**) with G_{i1}. Hydrogen bonds are indicated by red dashed lines. **d**, Different engagement modes of the αN-helix of G_q and G_{i1} upon coupling to MRGPRX2. The relative displacements of G_q with respect to G_{i1} are indicated by arrows. **e**, Detailed view of the interaction of MRGPRX2 ICL2 with G_q. Hydrogen bonds are indicated by red dashed lines.

E164$^{4.60}$ impaired the efficacy of (*R*)-ZINC-3573 (Fig. 1j) and greatly reduced the potencies of peptide agonists (Fig. 1i, Extended Data Fig. 5e–g). As many positively charged peptides and cationic small molecules activate MRGPRX2[18], ionic interactions involving these two acidic residues may be crucial for agonist recognition and activation of MRGPRX2. Consistent with the pose observed in this structure, most alanine mutations in the (*R*)-ZINC-3573 pocket greatly reduced the efficacy of (*R*)-ZINC-3573 (Fig. 1j, Supplementary Table 1).

On the intracellular side, MRGPRX2 displayed a similar TM6 disposition in G_{i1}- and G_q-coupled structures (Extended Data Fig. 4c, e). The cytoplasmic distance between TM3 and TM6 is approximately 15 Å in both structures, consistent with other active-state and G-protein-coupled family A GPCR structures[19–21] and distinct from inactive-state, G-protein-uncoupled-state structures[17,22]. Both G_{i1} and G_q form extensive hydrophobic and electrostatic interactions with the core through the α5-helix (Fig. 2a). However, they adopt different conformations upon coupling to MRGPRX2 (Fig 2a–e, Extended Data Fig. 4c–g). The α5-helix C terminus of G_q engages the intracellular cavity of MRGPRX2 about 2 Å closer to TM6 compared to what is observed with G_{i1} (Fig. 2a), probably owing to an interaction of the bulky Y243$^{H5.23}$ of G_q with the TM2–TM3 interface of MRGPRX2.

Outside the receptor core is the clearly resolved intracellular loop 3 (ICL3), which forms extensive interactions with G_{i1} (Fig. 2b, Extended Data Fig. 4g). Specifically, R214^{ICL3} extends downwards and forms hydrogen bonds with the side chain of E318 and the carbonyl group of I319 of G_{i1}. In addition, L216^{ICL3} engages the G_{i1} α5-helix residues I344 and L348 through hydrophobic interactions (Fig. 2b). Mutations of R214^{ICL3} and L216^{ICL3} impaired the efficacy of agonist-stimulated G_{i1} activation (Extended Data Fig. 4h, i, Supplementary Table 2), suggesting that ICL3 of MRGPRX2 has a role in G_{i1} coupling. By contrast, ICL3 was not resolved in G_q-coupled structures (Extended Data Fig. 4f).

Extensive interactions of ICL2 with the αN-helix of G_{i1} or G_q were also observed in both MRGPRX2 structures (Fig. 2c–e). In the G_{i1}-coupled MRGPRX2, R138^{ICL2} points downwards to the αN-helix of G_{i1} and hydrogen bonds with the backbone carbonyl of E33. The carbonyl group of C139^{ICL2} introduces an extra hydrogen bond with R32 of G_{i1} (Fig. 2c). In the G_q-coupled structure, the αN-helix of G_q shifts 6.6 Å outwards compared with that of G_i and interacts with ICL2 through a distinct hydrogen-bond network (Fig. 2d, e). In both G_q and G_{i1}-coupled structures, I135^{ICL2} is buried in a hydrophobic groove formed mainly by the αN–β1 junction, the β2–β3 loop and the α5-helix of the G protein (Fig. 2c, e), and has a key role in G-protein activation (Extended Data Fig. 4j–m, Supplementary Table 2).

Discovery of MRGPRX2 antagonists

The development of a selective MRGPRX2 antagonist has substantial therapeutic potential. We were able to confirm the activity of compound 2 (ZINC16991592, '1592) from a previous study[23] at MRGPRX2, finding that '1592 had an inhibition constant (K_i) value of 189 nM (Fig. 3a, Supplementary Table 3). Searching the ZINC database (http://zinc15.docking.org) and two rounds of analogue modelling in the ultra-large make-on-demand libraries (Supplementary Data 1, Fig. 3a, Extended Data Fig. 7a, b, Supplementary Tables 4, 5), we ultimately obtained optimized compounds C9-6 and C9, with K_i values of 58 nM and 43 nM, respectively (Fig. 3b, Supplementary Table 3). We found that C9-6 and C9 are inverse agonists for MRGPRX2 (Fig. 3c). A recent study suggested that substance P-induced inflammation and pain is at least partially mediated by MRGPRX2 rather than its canonical receptor, neurokinin-1 receptor[3] (NK1R). We demonstrated both C9-6 and C9 could inhibit MRGPRX2 activation stimulated by various endogenous peptides (Extended Data Fig. 7c), including substance P (Fig. 3d). Off-target profiling revealed no significant activity at a number of GPCRs, ion channels and transporters when screened at 10 μM (Supplementary Excel File 1). In addition, C9-6 and C9 display no antagonist activity towards NK1R (Fig. 3e) or MRGPRX4 (Fig. 3f, Supplementary Table 3), revealing them as potent and selective MRGPRX2 inverse agonists. Compound C9 and the inactive control C7 were further tested in mast cell degranulation assay; C9 inhibited (*R*)-ZINC-3573-stimulated LAD2 human mast cell degranulation in a concentration-dependent manner (Fig. 3g).

Discovery of a potent MRGPRX4 agonist

Whereas the two acidic residues critical for the cationic agonist recognition in MRGPRX2 are conserved in the highly similar MRGPRX family

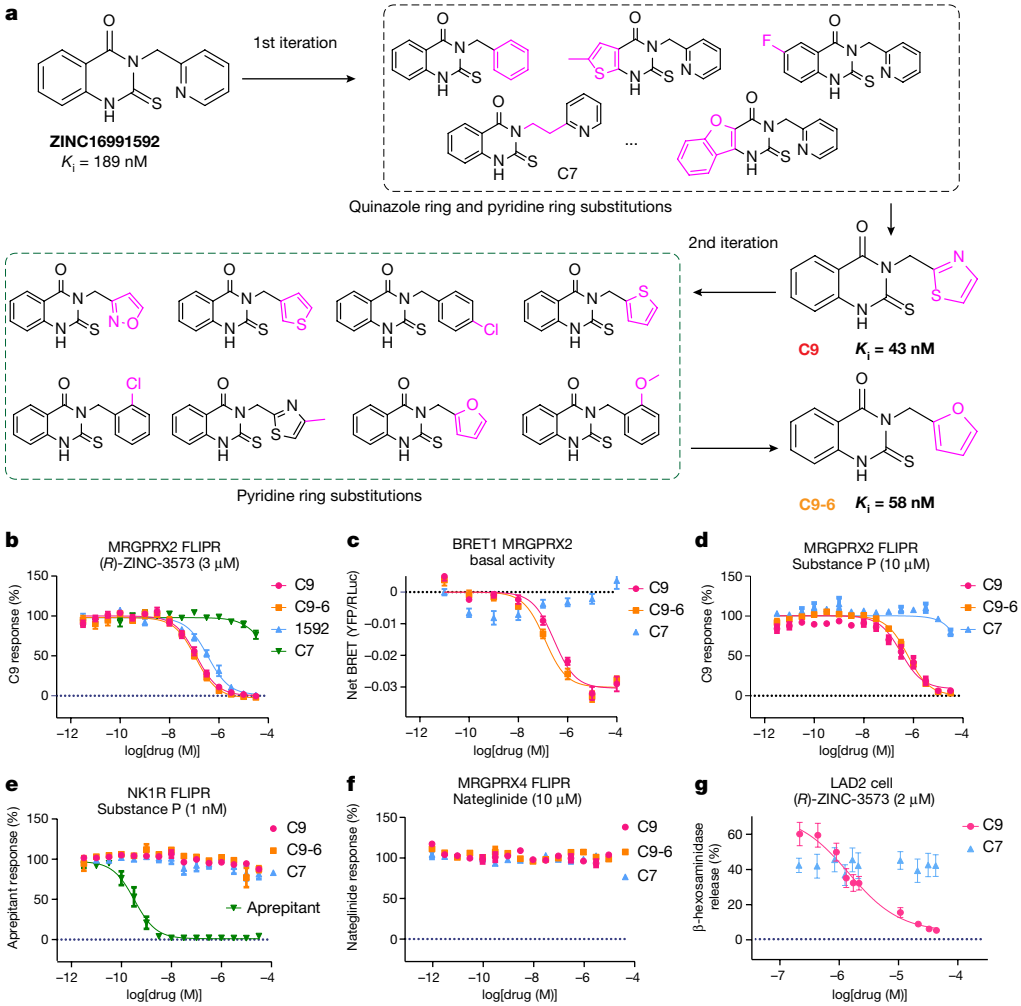

Fig. 3 | Discovery of MRGPRX2-selective inverse agonists. a, Overview of the analogue optimization towards C9 and C9-6. **b**, C9 and C9-6 show improved antagonist activity for MRGPRX2 when compared with the parent compound '1592. C7 represents an inactive control. The (*R*)-ZINC-3573 concentration producing 80% of the maximum effect (EC_{80}) (3 μM) was added in the antagonist-mode FLIPR Ca^{2+} assay. Data are mean ± s.e.m. of $n = 3$ biological replicates. **c**, C9 and C9-6 inhibit the basal recruitment of G_q by MRGPRX2 and exhibit inverse agonist activities. Data are mean ± s.e.m. of $n = 3$ biological replicates. **d**, C9 and C9-6 inhibit substance P (10 μM)-stimulated MRGPRX2 activation in a FLIPR Ca^{2+} assay. Data are mean ± s.e.m. of $n = 3$ biological replicates. **e**, **f**, C9 and C9-6 exhibit no antagonist activity towards NK1R (**e**) and MRGPRX4 (**f**) in the FLIPR Ca^{2+} assay. C7 is used as a negative control. Data are mean ± s.e.m. of $n = 3$ biological replicates. **g**, C9 inhibits MRGPRX2-mediated LAD2 mast cell activation. Data are mean ± s.e.m. Samples were run in quadruplicate with $n = 2$ biological replicates.

receptors (Supplementary Fig. 1), the other three MRGPRX receptors are not reported to respond to cationic agonists. By contrast, MRGPRX4 binds to negatively charged bile acids[4,5]. The differential sensitivities of charged agonists prompted us to solve the MRGPRX4 structure. Unfortunately, there were no sufficiently potent agonists available to stabilize MRGPRX4.

We previously identified the antidiabetic drug nateglinide, which modulates Kir6.2/SUR1 potassium channels, as a low micromolar agonist for MRGPRX4[12] and used it to demonstrate that MRGPRX4 is a G_q-coupling receptor. Upon reviewing the initial medicinal chemistry studies of nateglinide[24], we synthesized a nateglinide analogue (referred to as X4-1) that was reported to be inactive at the potassium channel (Fig. 4a, Supplementary Data 2); X4-1 did not substantially alter the efficacy or potency when compared to nateglinide (Fig. 4b, Supplementary Table 6). An X4-1 analogue with reverse stereochemistry (X4-2) showed no agonist activity on MRGPRX4, while further modification by the addition of hydrophobic ethyl substituents to the cycloheptyl group of X4-1, namely X4-3, slightly increased MRGPRX4 activity (Fig. 4b, Supplementary Table 6). We then searched the ZINC database[25] (http://zinc15.docking.org), prioritizing analogues with larger, bulkier and more hydrophobic substituents than X4-1. Following extensive screening of analogues, we identified compound MS47134 as a potent MRGPRX4 agonist (half-maximal effective concentration (EC_{50}) = 149 nM) (Fig. 4b, Supplementary Table 6) with 47-fold improved selectivity for MRGPRX4 over the Kir6.2/SUR1 potassium channel (Extended Data Fig. 8a–i). Off-target profiling of MS47134 at 320 GPCRs showed activity only at MRGPRX4 and MRGPRX1 with no appreciable agonist or antagonist activity at the other 318 tested GPCRs (Extended Data Fig. 8j). The activity against MRGPRX1 was not replicated in subsequent concentration–response assay (Supplementary Fig. 2); thus, MS47134 represents a selective MRGPRX4 agonist.

Structure of MRGPRX4–G_q complex

We then used MS47134 to obtain an MRGPRX4–MS47134–G_q structure at a resolution of 2.6 Å (Extended Data Fig. 2). The overall structure of MRGPRX4 resembles MRGPRX2 at the intracellular side (Extended Data Fig. 9a, d). However, the extracellular tip of TM3 in MRGPRX4 was displaced 5.2 Å inward compared with MRGPRX2, resulting in a

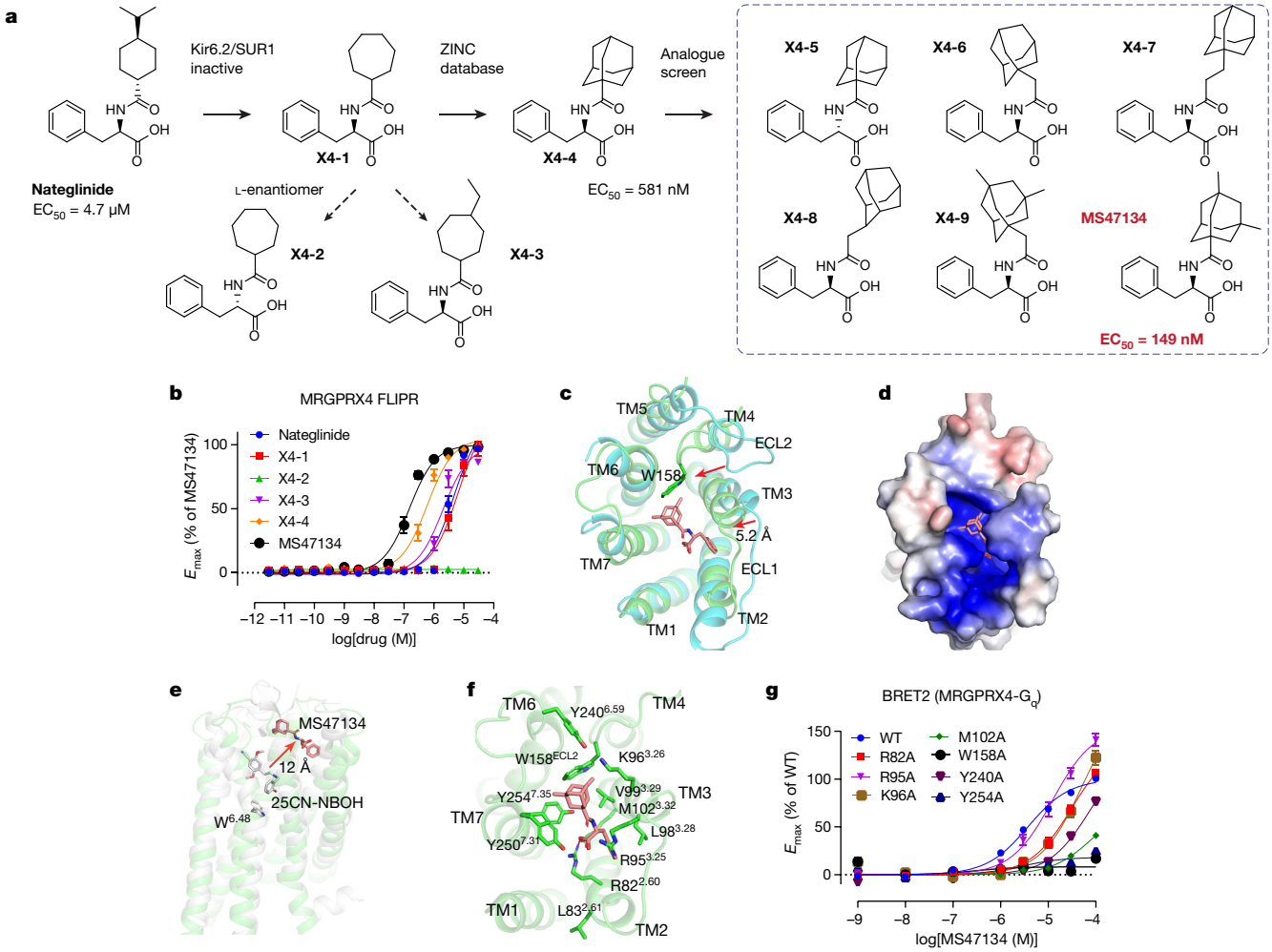

Fig. 4 | Agonist discovery and the cryo-EM structure of MRGPRX4. **a**, Overview of compound optimization leading to the discovery of MS47134. **b**, MS47134 exhibited increased potency as a MRGPRX4 agonist in the FLIPR Ca^{2+} assay compared with nateglinide. Data are mean ± s.e.m. of $n = 3$ biological replicates. **c**, Structural comparison of MRGPRX4 and MRGPRX2. Displacements of the extracellular part of MRGPRX4 relative to MRGPRX2 are highlighted with red arrows. MRGPRX4 and MRGPRX2 are shown in green and cyan, respectively. MS47134 is shown as salmon sticks. **d**, Electrostatic surface representation of the MRGPRX4 extracellular pocket calculated using the APBS plugin in PyMOL. Red, negative (−5 kT e^{-1}); blue, positive (+5 kT e^{-1}). **e**, MS47134 binds to MRGPRX4 on the extracellular side far from the canonical toggle switch $W^{6.48}$ in 5-HT_{2A}R. MS47134 and the 5-HT_{2A}R agonist 25CN-NBOH are shown as sticks. **f**, Molecular interactions in the MS47134 pocket with surrounding residues shown as sticks. **g**, Alanine substitution on key residues in the MS47134 pocket impairs MS47134 mediated G_q activation. Data are mean ± s.e.m. of $n = 3$ biological replicates.

compact binding pocket for MS47134 (Fig 4c). Additionally, the ECL2 of MRGPRX4 shifts into the orthosteric pocket with $W158^{ECL2}$ inserted right between TM3 and TM6 (Fig. 4c), making $D177^{5.38}$ and $E157^{4.60}$, the two equivalent acidic residues that are critical for cationic agonist recognition in MRGPRX2, solvent-inaccessible (Extended Data Fig. 9e, f). This could explain the apparent insensitivity of MRGPRX4 to cationic agonists. By contrast, the MRGPRX4 binding pocket has an overall positive electrostatic potential surface (Fig. 4d), which is likely to facilitate the binding of its endogenous agonists—negatively charged bile acids[4]. Because the agonist binds very close to the extracellular surface, the electron microscopy density for the phenyl group of MS47134 was not well-resolved in the complex map. We were then able to do a local refinement for the receptor-only region during revision, substantially improving the map quality with a clear MS47134 density for unambiguous modelling. In this improved model, MS47134 binds to MRGPRX4 distantly from the canonical orthosteric binding site seen in biogenic amine receptors (Fig. 4e, Extended Data Fig. 6c), with its 3,5-dimethyl-adamantyl group anchored by $K96^{3.26}$, $V99^{3.29}$, $W158^{ECL2}$, $Y240^{6.59}$, $Y250^{7.31}$ and $Y254^{7.35}$ (Fig. 4f). The carboxyl group of MS47134 mainly forms charge interactions with $R82^{2.60}$, while its phenyl group interacts with $L98^{3.28}$, $R95^{3.25}$, $M102^{3.32}$ and $R82^{2.60}$ through non-polar interactions (Fig. 4f). Mutagenesis studies support the pose of MS47134 in the binding pocket, as most of the mutations surrounding MS47134 greatly affected its potency (Fig. 4g, Supplementary Table 7). Of note, $Leu83^{2.61}$—which is annotated in the reference sequence—is highly polymorphic and is replaced by $Ser83^{2.61}$ in many individuals. A L83S mutation greatly attenuated the potency of both MS47134 and nateglinide (Supplementary Fig. 3), suggesting that side effects of MRGPRX4-mediated itch may be less common in individuals with the L83S mutation.

The interactions between MRGPRX4 and G_q resemble those in the MRGPRX2–G_q structure (Extended Data Fig. 9a–d), the only major difference being that $Y243^{H5.23}$ of G_q adopts different side-chain conformations to interact with $Y130^{ICL2}$ upon coupling to MRGPRX4, probably resulting from the strong interaction between $V61^{2.39}$ of MRGPRX4 and $Y243^{H5.23}$ of G_q (Extended Data Fig. 9g). A $Y130^{ICL2}$A mutation reduced the agonist potency of MS47134 while the $Y137^{ICL2}$A mutation in MRGPRX2 has little effect (Extended Data Fig. 9h, i), suggesting that the interaction between $Y130^{ICL2}$ and G_q α5-helix residue $Y243^{H5.23}$ is more important for G_q activation in MRGPRX4.

Discussion

The cryo-EM structures of MRGPRX2 and MRGPRX4 highlight unique aspects of signalling by the MRGPRX subfamily of GPCRs, and provide a template for the discovery and mechanistic understanding of selective chemical tools with which their function can be probed to inform the design of new therapeutic agents. From a signalling perspective, the MRGPRXs lack many of the canonical motifs associated with signalling and ligand recognition in family A GPCRs. The structures reveal that MRGPRX2 and MRGPRX4 agonists bind close to the extracellular solvent, over 10 Å 'higher' than the orthosteric sites of most family A GPCRs (Extended Data Fig. 6c). This in turn reflects the replacement of the conserved 'toggle' residue $W^{6.48}$ by $G^{6.48}$ in both receptors, shifting TM6 towards TM3 and precluding agonist binding at the canonical site. As MRGPRX2 and MRGPRX4 agonists are located far away from $G^{6.48}$, $G^{6.48}$ no longer acts as a toggle switch to sense the ligand and initiate conformational changes required for receptor activation. This suggests that there is a unique ligand-transduction mechanism in MRGPRX family receptors, which might require the formation of a MRGPR-specific TM4–TM5 disulfide bond.

MRGPRX2 and MRGPRX4 have been implicated in mediating itch[4,26], neurogenic inflammation[3], atopic dermatitis[27], ulcerative colitis[28], preference for menthol cigarettes[29], pain[30] and several mast cell-mediated responses[31]. The relatively potent agonists and antagonists described here provide chemical probes to explore the biology of these receptors, and the structures will accelerate the search for specific therapeutic agents targeting MRGPRs.

Online content

Any methods, additional references, Nature Research reporting summaries, source data, extended data, supplementary information, acknowledgements, peer review information; details of author contributions and competing interests; and statements of data and code availability are available at https://doi.org/10.1038/s41586-021-04126-6.

1. Zylka, M. J., Dong, X., Southwell, A. L. & Anderson, D. J. Atypical expansion in mice of the sensory neuron-specific Mrg G protein-coupled receptor family. *Proc. Natl Acad. Sci. USA* **100**, 10043–10048 (2003).
2. McNeil, B. D. et al. Identification of a mast-cell-specific receptor crucial for pseudo-allergic drug reactions. *Nature* **519**, 237–241 (2015).
3. Green, D. P., Limjunyawong, N., Gour, N., Pundir, P. & Dong, X. A mast-cell-specific receptor mediates neurogenic inflammation and pain. *Neuron* **101**, 412–420.e413 (2019).
4. Yu, H. et al. MRGPRX4 is a bile acid receptor for human cholestatic itch. *eLife* **8**, e48431 (2019).
5. Meixiong, J., Vasavda, C., Snyder, S. H. & Dong, X. MRGPRX4 is a G protein-coupled receptor activated by bile acids that may contribute to cholestatic pruritus. *Proc. Natl Acad. Sci. USA* **116**, 10525–10530 (2019).
6. Chompunud Na Ayudhya, C., Roy, S., Alkanfari, I., Ganguly, A. & Ali, H. Identification of gain and loss of function missense variants in MRGPRX2's transmembrane and intracellular domains for mast cell activation by substance P. *Int. J. Mol. Sci.* **20**, 5247 (2019).
7. Ikoma, A., Steinhoff, M., Stander, S., Yosipovitch, G. & Schmelz, M. The neurobiology of itch. *Nat. Rev. Neurosci.* **7**, 535–547 (2006).
8. Greaves, M. W. & Wall, P. D. Pathophysiology of itching. *Lancet* **348**, 938–940 (1996).
9. Liu, Q. et al. Sensory neuron-specific GPCR Mrgprs are itch receptors mediating chloroquine-induced pruritus. *Cell* **139**, 1353–1365 (2009).
10. Lembo, P. M. et al. Proenkephalin A gene products activate a new family of sensory neuron–specific GPCRs. *Nat. Neurosci.* **5**, 201–209 (2002).
11. Azimi, E. et al. Dual action of neurokinin-1 antagonists on Mas-related GPCRs. *JCI Insight* **1**, e89362 (2016).
12. Kroeze, W. K. et al. PRESTO-Tango as an open-source resource for interrogation of the druggable human GPCRome. *Nat. Struct. Mol. Biol.* **22**, 362–369 (2015).
13. Lansu, K. et al. In silico design of novel probes for the atypical opioid receptor MRGPRX2. *Nat. Chem. Biol.* **13**, 529–536 (2017).
14. Subramanian, H. et al. β-Defensins activate human mast cells via Mas-related gene *X2*. *J. Immunol.* **191**, 345–352 (2013).
15. Olsen, R. H. J. et al. TRUPATH, an open-source biosensor platform for interrogating the GPCR transducerome. *Nat. Chem. Biol.* **16**, 841–849 (2020).
16. English, J. G. et al. VEGAS as a platform for facile directed evolution in mammalian cells. *Cell* **178**, 748–761.e717 (2019).
17. Wacker, D. et al. Structural features for functional selectivity at serotonin receptors. *Science* **340**, 615–619 (2013).
18. Lu, L., Kulka, M. & Unsworth, L. D. Peptide-mediated mast cell activation: ligand similarities for receptor recognition and protease-induced regulation. *J. Leukoc. Biol.* **102**, 237–251 (2017).
19. Che, T. et al. Structure of the nanobody-stabilized active state of the kappa opioid receptor. *Cell* **172**, 55–67.e15 (2018).
20. Che, T. et al. Nanobody-enabled monitoring of kappa opioid receptor states. *Nat. Commun.* **11**, 1145 (2020).
21. Rasmussen, S. G. F. et al. Crystal structure of the β2 adrenergic receptor–G_s protein complex. *Nature* **477**, 549–555 (2011).
22. Rosenbaum, D. M. et al. GPCR engineering yields high-resolution structural insights into β2-adrenergic receptor function. *Science* **318**, 1266–1273 (2007).
23. Ogasawara, H., Furuno, M., Edamura, K. & Noguchi, M. Novel MRGPRX2 antagonists inhibit IgE-independent activation of human umbilical cord blood-derived mast cells. *J. Leukoc. Biol.* **106**, 1069–1077 (2019).
24. Shinkai, H. et al. *N*-(cyclohexylcarbonyl)-D-phenylalanines and related compounds. A new class of oral hypoglycemic agents. 2. *J. Med. Chem.* **32**, 1436–1441 (1989).
25. Irwin, J. J. & Shoichet, B. K. ZINC–a free database of commercially available compounds for virtual screening. *J. Chem. Inf. Model.* **45**, 177–182 (2005).
26. Meixiong, J. et al. Identification of a bilirubin receptor that may mediate a component of cholestatic itch. *eLife* **8**, e44116 (2019).
27. Azimi, E., Reddy, V. B. & Lerner, E. A. Brief communication: MRGPRX2, atopic dermatitis and red man syndrome. *Itch (Phila)* **2**, e5 (2017).
28. Chen, E. et al. Inflamed ulcerative colitis regions associated to MRGPRX2-mediated mast cell degranulation and cell activation modules, defining a new therapeutic target. *Gastroenterology* **160**, 1709–1724 (2021).
29. Kozlitina, J. et al. An African-specific haplotype in MRGPRX4 is associated with menthol cigarette smoking. *PLoS Genet.* **15**, e1007916 (2019).
30. Li, Z. et al. Targeting human Mas-related G protein-coupled receptor X1 to inhibit persistent pain. *Proc. Natl Acad. Sci. U.S.A.* **114**, E1996–E2005 (2017).
31. Thapaliya, M., Chompunud Na Ayudhya, C., Amponnawarat, A., Roy, S. & Ali, H. Mast cell-specific MRGPRX2: a key modulator of neuro-immune interaction in allergic diseases. *Curr. Allergy Asthma Rep.* **21**, 3 (2021).

Methods

Generation of MRGPRX2, MRGPRX4, G_{i1} heterotrimer and G_q heterotrimer constructs

Genes for human MRGPRX2 (UniProtKB-Q96LB1) and human MRGPRX4 (UniProtKB-Q96LA9) were individually cloned into a modified pFastBac1 vector which contains a hemagglutinin (HA) signal peptide followed by a Flag-tag, His_{10}-tag, and a TEV protease site at the N terminus. To facilitate protein expression and subsequent purification, thermostabilized apocytochrome b562RIL (BRIL) and HRV3C protease sites were introduced at the N terminus of the receptor. For G_q protein, we used the same mini-$G\alpha_{qi}$N heterotrimer construct as used for the $5HT_{2A}R$–G_q complex[32]. For G_{i1} protein, a dominant-negative human $G\alpha_{i1}$ and $G\beta_1\gamma_2$ subunits were cloned into pFastbac1 and pFastDual vector individually as previously reported[33].

Expression of receptor–G protein complex

The Bac-to-Bac Baculovirus Expression System (Invitrogen) was used to generate recombinant baculovirus for protein expression. Prior to infection, viral titres were determined by flow-cytometric analysis of cells stained with gp64-PE antibody (Expression Systems). For the MRGPRX2–G_{i1} complex, MRGPRX2, dominant-negative G_{i1} and $G\beta_1\gamma_2$ were co-expressed by infecting Tni cells at a density of 2 million cells per ml with P1 baculovirus at multiplicity of infection (MOI) ratio of 2.5:1:1. Cells were collected by centrifugation 48 h after infection and stored at −80 °C for future use. For the MRGPRX2–G_q and MRGPRX4–G_q complex, both MRGPRX2 and MRGPRX4 were co-expressed with mini-$G\alpha_{qi}$N heterotrimer by infecting Tni cells at a density of 2 million cells per ml with P1 baculovirus at an MOI ratio of 3:1.5, respectively. Cells were collected by centrifugation 48 h after infection and stored at −80 °C for future use.

scFv16 expression and purification

The scFv16 gene was cloned into a modified pFastBac1 vector, expressed and purified as previously reported[34] . In brief, supernatant containing secreted scFv16 from baculovirus-infected Sf9 insect cells was collected by centrifugation at 96 h after infection. The pH of the medium was adjusted to 7.8 by adding Tris powder. Chelating agents were quenched by addition of 1 mM nickel chloride and 5 mM calcium chloride and stirring at room temperature for 1 h. After another centrifugation, the supernatant was incubated with 1 ml His60 Ni Superflow Resin (Takara) overnight at 4 °C. The resin was collected next day and washed with 20 column volumes of 20 mM HEPES pH 7.5, 500 mM NaCl, 10 mM imidazole. The protein was eluted with 20 mM HEPES pH 7.5, 100 mM NaCl, 250 mM imidazole and further purified by size-exclusion chromatography using a Superdex 200 16/60 column (GE healthcare). The peak fraction was collected and concentrated to 2 mg ml^{-1} for future use.

Receptor–G protein complex purification

The pellet of cells expressing MRGPRX2–G_q complex was thawed on ice and incubated with a buffer containing 20 mM HEPES pH 7.5, 50 mM NaCl, 1 mM $MgCl_2$, 2.5 units of Apyrase (NEB) and proteinase inhibitor at room temperature. After 1.5 h, the cell suspension was homogenized with a dounce homogenizer. Membranes were collectedby centrifugation at 25,000 rpm for 30 min using a Ti45 rotor (Beckman) and solubilized using 40 mM HEPES pH 7.5, 100 mM NaCl, 5% (w/v) glycerol, 0.6% (w/v) lauryl maltose neopentyl glycol (LMNG), 0.06% (w/v) cholesteryl hemisuccinate (CHS) for 5 h at 4 °C with 500 μg scFv16. The solubilized proteins in the supernatants were isolated by ultracentrifugation at 32,000 rpm for 30 min using a Ti70 rotor, and then incubated overnight at 4 °C with Talon IMAC resin (Clontech) and 20 mM imidazole. The resin was collected next day and washed with 25 column volumes buffer containing 20 mM HEPES pH 7.5, 100 mM NaCl, 30 mM imidazole, 0.01% (w/v) LMNG, 0.001% (w/v) CHS and 5% glycerol. The protein was then eluted using the same buffer supplemented with 250 mM imidazole. Eluted protein was concentrated and subjected to size-exclusion chromatography on a Superdex 200 Increase 10/300 column (GE Healthcare) that was pre-equilibrated with 20 mM HEPES pH 7.5, 100 mM NaCl, 100 μM TCEP, 0.00075% (w/v) LMNG, 0.00025 (w/v) glyco-diosgenin (GDN) and 0.00075% (w/v) CHS. Peak fractions were collected and incubated with 15 μl of His-tagged PreScission protease (GeneScript) and 2 μl PNGase F (NEB) at 4 °C overnight to remove the N-terminal BRIL and potential glycosylation. The protein was concentrated and further purified next day by size-exclusion chromatography using a same buffer. Peak fractions were collected and concentrated to 3–5 mg ml^{-1}. 200 μM (*R*)-ZINC-3573 or 100 μM Cortistantin-14 was added to the concentrated complex sample and incubate at cold room for 2 h prior to grid-making. The same protocol was also used for the purification of MRGPRX2-G_{i1} complex, except that the N-terminal Bril was not removed by adding PreScission protease. The MRGPRX4–G_q complex was purified using a same protocol as for the MRGPRX2–G_{i1} complex except 20 μM MS47134 was added throughout the purification to stabilize the complex. The protein was then concentrated to 5 mg ml^{-1} and incubated with 200 μM MS47134 for 2 h prior to grid making.

Cryo-EM data collection and 3D reconstitution

The samples (3.2 μl) were applied to glow discharged Quantifoil R1.2/1.3 Au300 holey carbon grids (Ted Pella) individually and were flash frozen in a liquid ethane/propane (40/60) mixture using a Vitrobot mark IV (FEI) set at 4 °C and 100% humidity with a blot time range from 2.5 to 5 s. Images were collected using a 200 keV Talos Artica with a Gatan K3 direct electron detector at a physical pixel size of 0.91 Å. Micrograph-recorded movies were automatically collected using SerialEM using a multishot array[35]. Data were collected at an exposure dose rate of ~15 electrons per pixel per second as recorded from counting mode. Images were recorded for ~2.7 s in 60 subframes to give a total exposure dose of ~50 electron per $Å^2$. All subsequent three-dimensional classification and refinement steps were performed within cryoSPARC[36,37]. Following manual inspection and curation of the micrographs after patch-based motion correction and contrast transfer function (CTF) estimation, particles from each dataset were selected using Blob particle picker and initial 2D classification yielded templates for subsequent template picking. A subset of the selected particles was used as a training set for Topaz and the particles were repicked from the micrographs using Topaz[38] and subjected to 2D and/or 3D classification. The picked particle coordinates from the three sets were merged yielding a subset of unique particle that survived 2D classification (that is, duplicates were removed with a radius of 100 pixels). Multiple rounds of multi-reference refinement resolved final stack of particles that produced a map with a resolution reported in Extended Data Table 1 (by Fourier shell correlation (FSC) using the 0.143 Å cut-off criterion)[39] after Global CTF refinement and post-processing including soft masking, B-factor sharpening in cryoSPARC and filtering by local resolution[40] to generate the post-processed sharpened map. Alternative post sharpening was performed on the two half-maps using deepEMhancer[41]. For MRGPRX4, a local refinement for the receptor only region was performed to improve the map quality for the ligand binding pocket to assist modelling. Angular orientation distribution was plotted using either cryoSPARC or cisTEM[42]. For more details see Extended Data Fig. 2, 3 and Extended Data Table 1.

Model building and refinement

Maps from deepEMhancer were used for map building, refinement and subsequent structural interpretation. The dominant-negative G_{i1} trimer model was adapted from the cryo-EM structure of the CB2–G_{i1} complex (PDB 6PT0)[43]. G_q trimer and scFv16 model was taken from the 5-$HT_{2A}R$–Gq complex (PDB 6WHA)[32]. The G proteins and scFv16 were docked into the cryo-EM map using Chimera[44]. The receptor model of MRGPRX2 and MRGPRX4 were manually built in Coot[45], followed by several rounds of real-space refinement using Phenix[46]. For cortistatin-14

in the MRGPRX2–G_q complex, residues 3–8 were modelled according to the map density. For the cortistatin-14 of MRGPRX2-G_{i1} complex, residues 2–6 were modelled. The binding pose of MS47134 is validated by GemSpot[47]. The model statistics was validated using Molprobity[48]. Structural figures were prepared using Chimera or Pymol (https://pymol.org/2/).

FLIPR Ca^{2+} assay

The FLIPR Ca^{2+} assay was used for all the drug screening for MRGPRX2, MRGPRX4 and NK1R. Tetracycline-inducible MRGPRX2 or MRGPRX4 stable cells (Flp-In T-REx–293 cells, derived from HEK 293 cells (ATCC, CRL 1573)) were maintained in DMEM containing 10% (v/v) FBS, 100 units ml^{-1} penicillin G, 100 μg ml^{-1} streptomycin, 100 μg ml^{-1} hygromycin B, and 15 μg ml^{-1} blasticidin[16]. Cells stably expressing NK1R were maintained in DMEM containing 10% (v/v) FBS, 100 units ml^{-1} penicillin G and 100 μg ml^{-1} streptomycin. On the day of assay, cells were plated into poly-L-lysine-coated 384-well black clear bottom cell culture plates with DMEM buffer, which is composed of 1% (v/v) dialysed FBS, 100 units ml^{-1} penicillin G, 100 μg ml^{-1} streptomycin with 1 μg ml^{-1} tetracycline at density of 20,000 cells in 40 μl per well for overnight. For NK1R stable cells, the same media used for MRGPRX2 or MRGPRX4 cells except the tetracycline were used. Medium was removed and cells were incubated with 20 μl of calcium dye (FLIPR Calcium 4 Assay Kit; Molecular Devices) diluted in assay buffer (1× HBSS, 2.5 mM probenecid, 20 mM HEPES, pH 7.4) for 1 h at 37 °C and 20 min at room temperature in the dark. To measure agonist activity of receptors, drug plates were prepared with increasing concentrations of test compound at 3 times the desired final concentration using drug buffer (1 × HBSS, 20 mM HEPES, 0.1% (w/v) BSA, pH 7.4). Once loaded in FLIPR (Molecular Devices), basal fluorescence was measured for 10 s, then 10 μl of test compounds were added followed by continued fluorescence measurement for an additional 120 s. When measuring antagonist activity of receptors, drug plates were prepared with increasing concentrations of test compound at 4 times the desired final concentration, added as above for their potential effects on basal levels for 120 s first, followed by a 15-min incubation before addition of 10 μl of 4× reference agonist at final concentration corresponding to the EC_{80}, which was indicated in the title of each graph. Data were normalized to percentage of the reference compound stimulation and analysed using nonlinear regression (log(agonist) versus response) in GraphPad Prism 9.0.

BRET2 assay

Agonist-stimulated G-protein activation of both MRGPRX2 and MRGPRX4 mutants was performed by BRET2 assay using transient transfection. HEK 293T cells were plated either in six-well dishes containing 350,000–400,000 cells per well, or 10-cm dishes at approximately 2 million per dish 20–24 h prior to transfection. The cells were then transfected with a 2:1:2:2 ratio of the receptor:GαrLuc8:Gβ:GγGFP DNA. *Trans*IT 2020 (Mirus biosciences) was used to complex the DNA at a ratio of 3 μl *Trans*IT per μg DNA, in OptiMEM (GIBCO) at a concentration of 10 ng DNA per μl OptiMEM. After 24 h, the cells were plated in poly-L-lysine-coated 96-well white clear bottom cell culture plates in plating media (DMEM + 1% dialyzed FBS) at a density of 40,000–50,000 cells in 200 μl per well and incubated overnight. The next day, the medium was carefully aspirated and cells were washed once with 60 μl of drug buffer (1× HBSS, 20 mM HEPES, 0.1% (w/v) BSA, pH 7.4), then 60 μl drug buffer containing coelenterazine 400a (Nanolight Technology) at 5 μM final concentration was added to each well and incubate for 5 min. Cells were then treated with 30 μl of 3× designated drug for an additional 5 min. After drug incubation, plates were read in an LB940 Mithras plate reader (Berthold Technologies) with a 395 nm (RLuc8-coelenterazine 400a) and 510 nm (GFP2) emission filters, and 1 s integration times. Each plate was read four times, and measurements from the fourth read were used in all analyses. BRET ratio was computed as the ratio of the GFP2 emission to rLuc8 emission. Data were normalized to percentage of wild-type stimulation with indicated reference agonist and analysed using nonlinear regression (log(agonist) versus response) in GraphPad Prism 9.0. The variable slope of log(agonist) versus normalized response was used for (*R*)-ZINC-3573 pocket mutations (D184A, E164A, W243A, F244A, L247A and W248A).

BRET1 assay

To test the inverse agonist activities of MRGPRX2 compounds, a BRET1 recruitment assay was performed. Human MRGPRX2 containing C-terminal *Renilla* luciferase (RLuc8), and Venus-tagged miniG_q were co-transfected at a ratio of 1:5 using HEK 293T cells. After 20–24 h, transfected cells were plated into poly-L-lysine coated 96-well clear bottom white plates in plating medium (DMEM + 1% (v/v) dialysed FBS). The next day, medium was decanted and cells were washed once with 60 μl drug buffer (1× HBSS, 20 mM HEPES, 0.1% (w/v) BSA, pH 7.4), then 60 μl drug buffer containing 5 μM coelenterazine h (Promega) was added to each well and incubate for 5 min. Cells were then treated with 30 μl of 3× designated drug for an additional 5 min. After drug incubation, plates were read in a LB940 Mithras plate reader (Berthold Technologies) for both luminescence at 485 nm and fluorescent eYFP emission at 530 nm for 1 s per well. The eYFP/RLuc ratio was calculated per well and the net BRET ratio was calculated and fitted using log(inhibitor) versus response in GraphPad Prism 9.0 to represent the inhibitory effect of MRGPRX2 compound.

Inhibition screen

Binding assays were performed by the NIMH Psychoactive Drug Screening program as described previously[49]. Detailed binding assay protocols are available at https://pdspdb.unc.edu/pdspWeb/content/UNC-CH%20Protocol%20Book.pdf.

Human mast cell activation assay

Mast cell activation was assessed by measuring extracellular release of β-hexosaminidase, a major component of mast cell granules. To assay human mast cell β-hexosaminidase release, LAD2 human mast cells were seeded at a concentration of 2×10^5 cells per well in 96-well plates in Tyrode's buffer (100 μl). Fifteen minutes before activation, varying concentrations of either C7 or C9 were added to the wells to reach a total volume of 190 μl. For activation, (*R*)-ZINC-3573 (10 μl, 2 μM) was added to each well for 30 min at 37 °C. Separate wells received either buffer (buffer control), 0.1% Triton X-100 (total β-hexosaminidase control), or (*R*)-ZINC-3573 alone (positive control) for the same amount of time. Thirty microlitres of the supernatant were then removed from each well and added to 10 μl of NAG substrate solution (*p*-nitrophenyl-*N*-acetyl-β-D-glucosaminide) and incubated for 1 h at 37 °C. Carbonate buffer (100 μl) was then added to each well and the absorbance of each well was immediately measured at 405 nm using a plate reader. Percent degranulation (%) was calculated as follows: (Treatment release − buffer release)/(total release − buffer release)) × 100. Samples were run in quadruplicate and each compoundwas assayed in at least two independent experiments. Data were analysed using GraphPad Prism 9.0.

GPCRome screening

Screening of compounds against the PRESTO-Tango GPCRome was accomplished using previously described methods with several modifications[50]. First, HTLA cells were plated in white 384-well clear bottom plates (Greiner) in DMEM (Sigma) with 1% (v/v) dialysed FBS and 10 U ml^{-1} penicillin-streptomycin (Gibco). After 24 h, the cells were transfected using PEI (Sigma) with an in-plate adapted method[51]. In brief, 17 ng per well PRESTO-Tango GPCR DNAs was resuspended in OptiMEM (Gibco) and hybridized with PEI prior to dilution and distribution into 384-well plates and subsequent addition to cells. After overnight incubation, MS47134 at 5× final concentration (3 μM) diluted

in DMEM with 1% (v/v) dialysed FBS were added to cells without replacement of the medium for 18–20 h. On the day of assay, medium and drug solution were dumped and loaded with 20 ul per well of Bright-Glo reagent (Promega). Plates were incubated for 20 min in the dark and the luminescence was counted for cells using SpectraMax Luminescence reader. Dopamine receptor D2 serves as an assay control with 0.1 mM Quinpirole. Data were analysed using GraphPad Prism 9.0. For MRGPRX1 for which activity was increased to more than threefold of basal levels of relative luminescence units, assays were repeated as a full dose–response assay. Activity for MRGPRX1 could not be confirmed, and we dismissed the activity seen in the single-point assay.

Surface expression

Cell-surface expression of MRGPRX2 and its mutants (or MRGPRX4 and its mutants) were measured using ELISA chemiluminescence. In brief, 48-h post-transfected cells plated in 384 white-well plates were fixed with 20 µl per well 4% (v/v) paraformaldehyde for 10 min at room temperature. The cells were then washed with 40 µl per well of phosphate buffered saline (PBS) twice then incubated with 20 µl per well 5% (v/v) BSA (bovine serum albumin) in PBS for 1 h. Cells are incubated with an anti-Flag–horseradish peroxidase-conjugated antibody (Sigma-Aldrich, A8592) diluted 1:10,000 in 5% (v/v) BSA in PBS for 1 h at room temperature. After washing 5 times with 80 µl per well PBS, 20 µl per well Super Signal Enzyme-Linked Immunosorbent Assay Pico Substrate (Thermo Fisher, 37070) was added to well for the development of signal and the luminescence was counted using a PHERAstar FSX (BMG Labtech). The luminescence signal was analysed in GraphPad Prism 9.0 and data were normalized to the signal of wild-type MRGPRX2 (or wild-type MRGPRX4). Cell-surface expression data of MRGPRX2 and MRGPRX4 mutants are shown in Supplementary Fig. 4. Up to a 50% reduction in protein expression was observed for some mutants. To determine how differences in receptor expression would affect the signalling, we transfected the cells with different amounts of wild-type MRGPRX2 pcDNA plasmid (50, 100, 200 and 400 ng). The resulting BRET2 curves of these transfections were nearly identical, with only modest changes of EC_{50} and E_{max} values observed (Supplementary Fig. 5), thereby demonstrating that the BRET2 assay is relatively insensitive to protein expression level.

Structure–activity relationship analysis for ZINC16991592 and X4-1

Preliminary structure–activity relationship (SAR) studies on the antagonist ZINC16991592 demonstrated that better antagonists could be developed against MRGPRX2 with higher selectivity. We sought to improve the affinity of ZINC16991592 in different scaffoldclasses. To do so, we used ZINC16991592 as template to search the 28 billion make-on-demand library of the Enamine REAL database usingSmallWorld similarity (https://sw.docking.org/, NextMove Software) and arthor substructure (http://arthor.docking.org) search engines. Of the 200,000 analogues resulting from the database search, these were filtered on the basis of molecular mass <320 Da and ECFP4-based Tanimoto coefficient (Tc) ≥0.35) against ZINC16991592. The resulting molecules were manually inspected for favourable changes in the compound with respect to ZINC16991592. During selection of molecules, we explored substitutions both on the pyridine ring as well as the quinazole ring. Substitutions in the pyridine ring involved moving around nitrogen in the pyridine ring, addition of halogens at *ortho*, *meta* or *para* positions, replacing the pyridine ring with benzene, isoxazole, 1-methylimidazole, thiazole, tetralone, thiophene and furan. Substitutions on the quinazole ring included replacement of 2-sulfanylidene-1 ,3-dihydroquinazolin-4-one with 1,3 dihydroquinazoline-2,4-dione or making the quinazole ring bigger with addition of another ring. Substitution of the pyridine ring with thiazole (C9) and furan (C9-6) resulted in the most potent and selective antagonist against MRGPRX2. The analogues with substitutions in the quinazole ring showed minimal antagonist activity against MRGPRX2, suggesting a tight SAR around this ring. All the compounds in MRGPRX2 SAR study were purchased from Enamine (Supplementary Data 1). To identify commercially available X4-1 analogues, we used substructure searches on the 2-acetylaminopropanoic acid core in ZINC15. Each substituent vector was systematically held constant or varied in multiple substructure searches to identify analogues, which were then clustered using ECFP4 fingerprints in RDKit. Diverse pharmacophoric feature representatives for each vector were identified for prioritization, using a design of experiment to ensure coverage of combinations. All the compound structures were drawn with ChemDraw 20.0.

Electrophysiology

HEK 293 cells were cultured in DMEM with 4.5 g l^{-1} glucose, L-glutamine and sodium pyruvate (Mediatech) containing 10% (v/v) FBS (Axenia BioLogix) and 1% (v/v) penicillin-streptomycin, at 37 °C and with 5% CO_2. Cells were lifted with trypsin-EDTA (Life Technologies) and passaged to 6-well plates (Warner Instruments) 3–4 days before recording. Transient transfection was performed with Lipofectamine 2000 (Thermo Fisher Scientific) 2 days before recording. The plasmids of human Kir6.2 and SUR1 were a gift from S.-L. Shyng (Oregon Health and Science University), and we fused mCherry fluorescent protein to the C-terminus of Kir6.2. The vector ratio for co-transfection of Kir6.2 to SUR1 was 1:10. Before recording, cells were lifted with trypsin-EDTA, kept in modified Tyrode's saline (140 mM NaCl, 5 mM KCl, 10 mM HEPES, 2 mM $CaCl_2$, 1 mM $MgCl_2$, 10 mM glucose, pH 7.2–7.3 with HCl), and were used within 8 h. For recording, an aliquot of cells was transferred to a recording chamber on a Nikon TE2000 Inverted Scope (Nikon Instruments), and transfection was confirmed with fluorescence microscopy. The pipette solution contained: 145 mM KCl, 1 mM $MgCl_2$, 5 mM EGTA, 2 mM $CaCl_2$, 20 mM HEPES, 0.3 mM K_2-ATP and 0.3 mM K_2-ADP. Patch borosilicate pipettes (Sutter Instruments) were pulled from a Sutter P-97 puller with resistances of 2–3 MΩ. Data were acquired using a Axopatch 200B amplifier controlled by Clampex 10.2 via Digidata 1550A (Axon Instruments), sampled at 10 kHz, filtered at 2 kHz. Membrane capacitance was around 15 pF. R_s was around 5 MΩ. The membrane potential was held at −80 mV and a ramp to +80 mV (1 mV ms^{-1}) was applied every second. Bath was switched to 150 mM KCl, 10 mM HEPES, 2 mM $CaCl_2$, and the chemical to be tested was dissolved in it and puffed with VC3-8xP pressurized perfusion system (ALA Science). For each solution, final pH was adjusted to 7.2–7.3 with KOH, NaOH or HCl, depending on the original pH and the major ion. The osmolality of each solution was 290–310 mOsm kg^{-1}. All recordings were performed at room temperature (22–24 °C). Unless specified, all chemicals were purchased from Sigma-Aldrich.

Reporting summary

Further information on research design is available in the Nature Research Reporting Summary linked to this paper.

Data availability

The coordinate and cryo-EM map of MRGPRX2–G_q–cortistatin-14, MRGPRX2–G_{i1}–cortistatin-14, MRGPRX2–G_q–(*R*)-ZINC-3573, MRGPRX2–G_{i1}–(*R*)-ZINC-3573 and MRGPRX4–G_q–MS47134 have been deposited to PDB (EMDB) with accession codes 7S8L (EMD-24896), 7S8M (EMD-24897), 7S8N (EMD-24898), 7S8O (EMD-24899) and 7S8P (EMD-24900), respectively. The cryoEM micrographs of MRGPRX4–G_q–MS47134, MRGPRX2–G_q–cortistatin-14, MRGPRX2–G_q–(*R*)-ZINC-3573, MRGPRX2–G_{i1}–cortistatin-14 and MRGPRX2–G_{i1}–(*R*)-ZINC-3573 have been deposited in the EMPIAR database (https://www.ebi.ac.uk/empiar/) with accession numbers EMPIAR-10852, EMPIAR-10853, EMPIAR-10854, EMPIAR-10855 and EMPIAR-10856, respectively. The MRGPRX2 antagonist C9 and C9-6 and negative control C7, and the MRGPRX4 agonist MS47134 and negative control X2-2 will be made available via Sigma-Millipore.

32. Kim, K. et al. Structure of a hallucinogen activated G_q-coupled 5-HT2a serotonin receptor. *Cell* **182**, 1574–1588.e1519 (2020).
33. Draper-Joyce, C. J. et al. Structure of the adenosine-bound human adenosine A_1 receptor-G_i complex. *Nature* **558**, 559–563 (2018).
34. Koehl, A. et al. Structure of the μ-opioid receptor–G_i protein complex. *Nature* **558**, 547–552 (2018).
35. Mastronarde, D. N. Automated electron microscope tomography using robust prediction of specimen movements. *J. Struct. Biol.* **152**, 36–51 (2005).
36. Punjani, A., Rubinstein, J. L., Fleet, D. J. & Brubaker, M. A. cryoSPARC: algorithms for rapid unsupervised cryo-EM structure determination. *Nat. Methods* **14**, 290–296 (2017).
37. Punjani, A., Zhang, H. & Fleet, D. J. Non-uniform refinement: adaptive regularization improves single-particle cryo-EM reconstruction. *Nat. Methods* **17**, 1214–1221 (2020).
38. Bepler, T., Kelley, K., Noble, A. J. & Berger, B. Topaz-Denoise: general deep denoising models for cryoEM and cryoET. *Nat. Commun.* **11**, 5208 (2020).
39. Rosenthal, P. B. & Henderson, R. Optimal determination of particle orientation, absolute hand, and contrast loss in single-particle electron cryomicroscopy. *J. Mol. Biol.* **333**, 721–745 (2003).
40. Heymann, J. B. & Belnap, D. M. Bsoft: image processing and molecular modelling for electron microscopy. *J. Struct. Biol.* **157**, 3–18 (2007).
41. Sanchez-Garcia, R. et al. DeepEMhacer: a deep learning solution for cryo-EM volume post-processing. *Commun. Biol.* **4**, 874 (2021).
42. Grant, T., Rohou, A. & Grigorieff, N. cisTEM, user-friendly software for single-particle image processing. *eLife* **7**, e35383 (2018).
43. Xing, C. et al. Cryo-EM structure of the human cannabinoid receptor CB2–G_i signaling complex. *Cell* **180**, 645–654.e613 (2020).
44. Pettersen, E. F. et al. UCSF Chimera—a visualization system for exploratory research and analysis. *J. Comput. Chem.* **25**, 1605–1612 (2004).
45. Emsley, P. & Cowtan, K. Coot: model-building tools for molecular graphics. *Acta Crystallogr. D* **60**, 2126–2132 (2004).
46. Adams, P. D. et al. PHENIX: a comprehensive Python-based system for macromolecular structure solution. *Acta Crystallogr. D* **66**, 213–221 (2010).
47. Robertson, M. J., van Zundert, G. C. P., Borrelli, K. & Skiniotis, G. GemSpot: a pipeline for robust modeling of ligands into cryo-EM maps. *Structure* **28**, 707–716.e703 (2020).
48. Chen, V. B. et al. MolProbity: all-atom structure validation for macromolecular crystallography. *Acta Crystallogr. D* **66**, 12–21 (2010).
49. Besnard, J. et al. Automated design of ligands to polypharmacological profiles. *Nature* **492**, 215–220 (2012).
50. Kroeze, W. K. et al. PRESTO-Tango as an open-source resource for interrogation of the druggable human GPCRome. *Nat. Struct. Mol. Biol.* **22**, 362–369 (2015).
51. Longo, P. A., Kavran, J. M., Kim, M. S. & Leahy, D. J. Transient mammalian cell transfection with polyethylenimine (PEI). *Methods Enzymol.* **529**, 227–240 (2013).

Acknowledgements This work was supported by NIH grants U24DA116195 (to B.L.R., B.K.S. and J.J.) and R35GM122481 (to B.K.S.), and by the Michael Hooker Distinguished Professorship to B.L.R. and NIH grant R01-DK121969, R01-DK121032 and R56-AI139620 to S.N.A. We thank J. Peck and J. Strauss of the UNC Cryo-EM Core Facility for technical assistance in this project. W.Y. is partly supported by Program for Breakthrough Biomedical Research funded by the Sandler Foundation, University of California, San Francisco. L.Y.J. is a Howard Hughes Medical Institute investigator. We thank S.-L. Shyng for the plasmids encoding human Kir6.2 and SUR1. The Titan X Pascal used for this research was kindly donated to J.F.F. by the NVIDIA Corporation.

Author contributions C.C. designed the experiments, performed the cloning, expression and purification of all the signalling complexes for cryo-EM study, built the models, refined the structures, performed BRET assays, participated in MRGPRX4 drug screening, analysed the data, and prepared the figures, tables and manuscript. H.J.K. designed experiments, performed drug screening and functional assays, analysed the data and assisted in preparing the manuscript, and reviewed and edited the manuscript. J.F.F. made the grids, and collected and processed the cryo-EM data. I.S. performed the SAR study for MRGPRX2. H.C., C.Z. and J.L. performed the SAR study for MRGPRX4, and designed, synthesized and characterized the MRGPRX4 agonists. W.Y. performed electrophysiology for Kir6.2/SUR1. R.H.G. assisted in the modelling and validation of structures. B.W.H. performed the LAD2 mast cell degranulation assay. B.J.B. assisted in the structure modelling. J.K. supported agonist discovery and optimization for MRGPRX4. S.T.S. performed the GPCRome assay. B.E.K. designed the G_q protein construct and assisted in the reviewing and editing of the manuscript. K.L., J.D.M., W.K.K., J.F.D. and R.H.J.O. performed the initial screening for MRGPRX4 compounds. J.G.E., X.-P.H. and Y.L. helped with the initial functional assays. S.Z. and K.K. assisted in the protein expression. S.N.A. guided the LAD2 mast cell degranulation assay. J.J. supervised the medicinal chemistry experiments. B.K.S. supervised the docking and compound design and edited the manuscript. L.Y.J. contributed to funding application. B.L.R. supervised the entire project, guided the structural and functional work and prepared the manuscript.

Competing interests A patent describing the MRGPRX2 antagonists has been filed by UCSF listing B.L.R., B.K.S., C.C., I.S. and H.J.K. as inventors.

Additional information

Supplementary information The online version contains supplementary material available at https://doi.org/10.1038/s41586-021-04126-6.

Correspondence and requests for materials should be addressed to Brian K. Shoichet, Jonathan F. Fay or Bryan L. Roth.

Peer review information *Nature* thanks the anonymous reviewer(s) for their contribution to the peer review of this work.

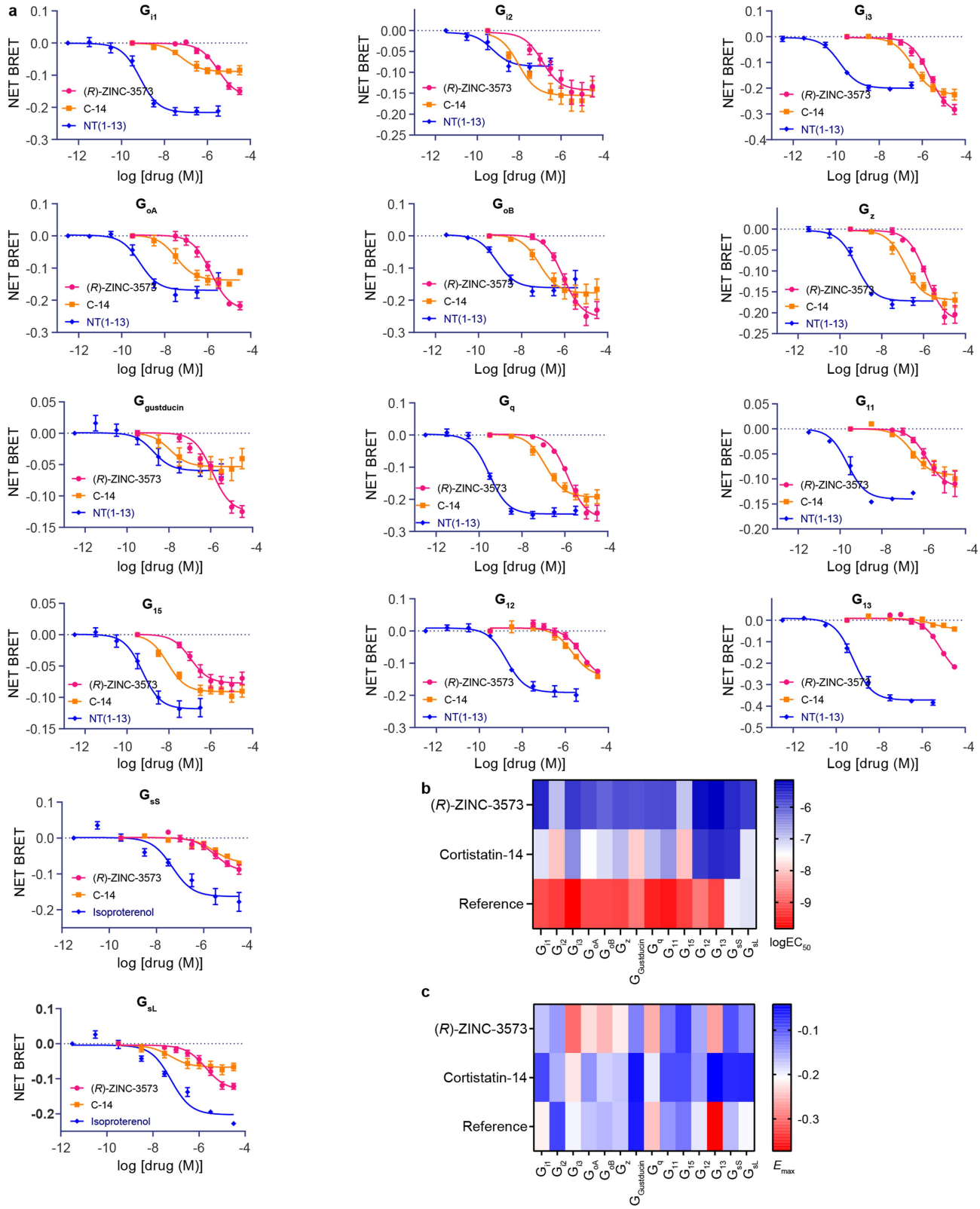

Extended Data Fig. 1 | MRGPRX2 transducerome screening using TRUPATH. a, MRGPRX2 effectively couples to 14 distinct G proteins upon stimulation of agonists (*R*)-ZINC-3573 and cortistatin-14 (C-14) in HEK 293T cells. Net BRET values of MRGPRX2 together with positive controls of either neurotensin receptor 1 (NTSR1, agonist NT1-13) or β_2AR (agonist isoproterenol) are shown in each panel. Data represent mean ± s.e.m. of $n = 3$ biological replicates. **b**, Heatmap of the relative log potency ($logEC_{50}$) of (*R*)-ZINC-3573 and cortistatin-14 for 14 distinct G proteins. **c**, Heatmap of the relative efficacy (E_{max}) of (*R*)-ZINC-3573 and cortistatin-14 for 14 distinct G proteins.

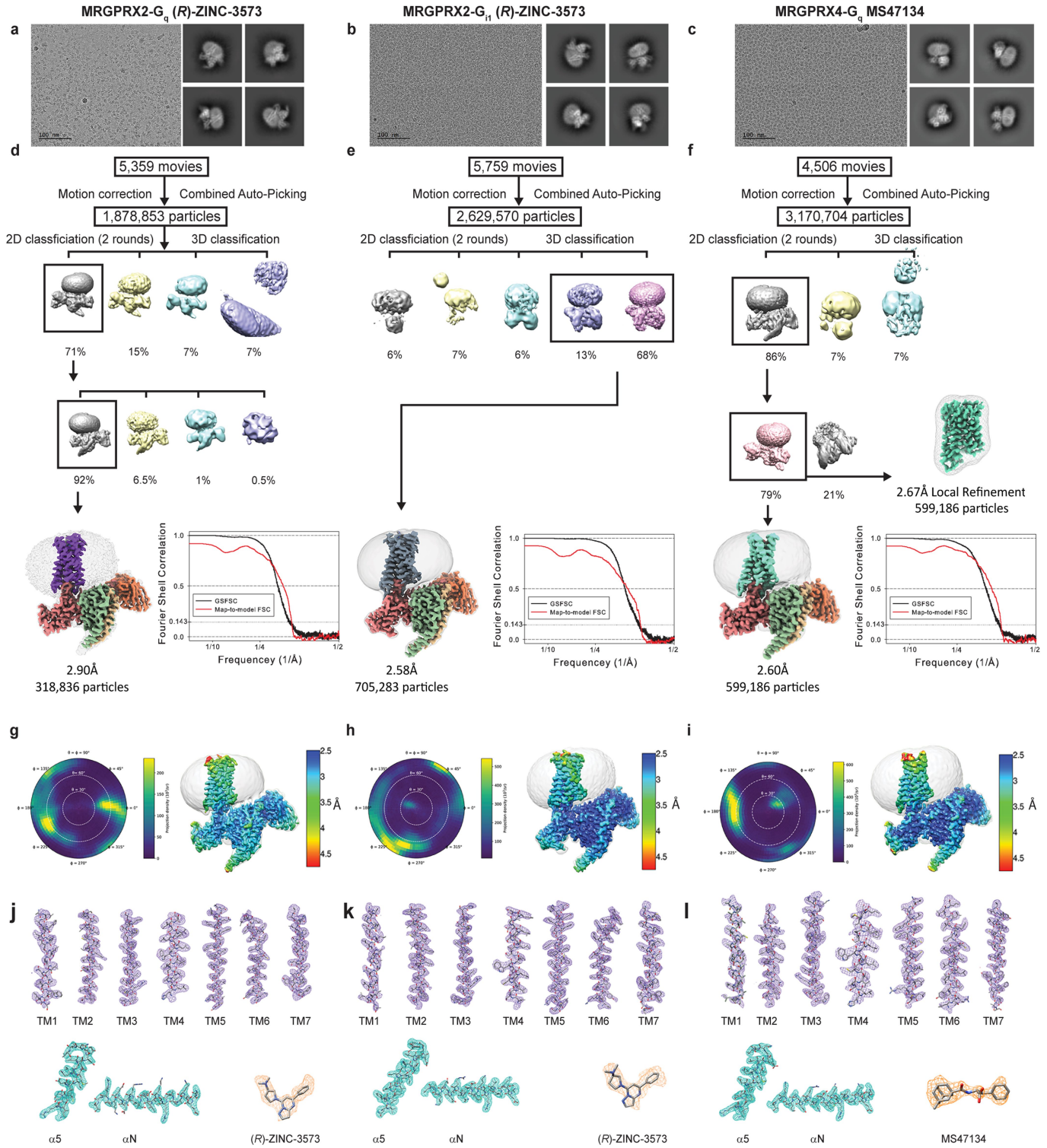

Extended Data Fig. 2 | CryoEM images and data-processing of MRGPRX2-G_q-(*R*)-ZINC-3573, MRGPRX2-G_{i1}-(*R*)-ZINC-3573 and MRGPRX4-G_q-MS47134 complex. a–**c**, Representative motion corrected cryo-EM micrographs (scale bar, 100 nm) of respective ligand bound GPCR heterotrimeric complex particles imaged at a nominal 45k x magnification and representative two-dimensional class averages. The experiment was repeated three times with similar result. The exact number of movies and particles used for each complex are shown in the flow chart. **d**–**f**, Flow chart of cryo-EM data processing, GSFSC plot of auto-masked final map (black) and map-to-model real-space cross correlation (red) as calculated form phenix.mtriage. **g**–**i**, Respective polar plots of particle angular distributions and local resolution estimations heat maps. **j**–**l**, Local cryo-EM density maps of TM1-7, respective ligands, and α5 and αN helix of respective G-protein.

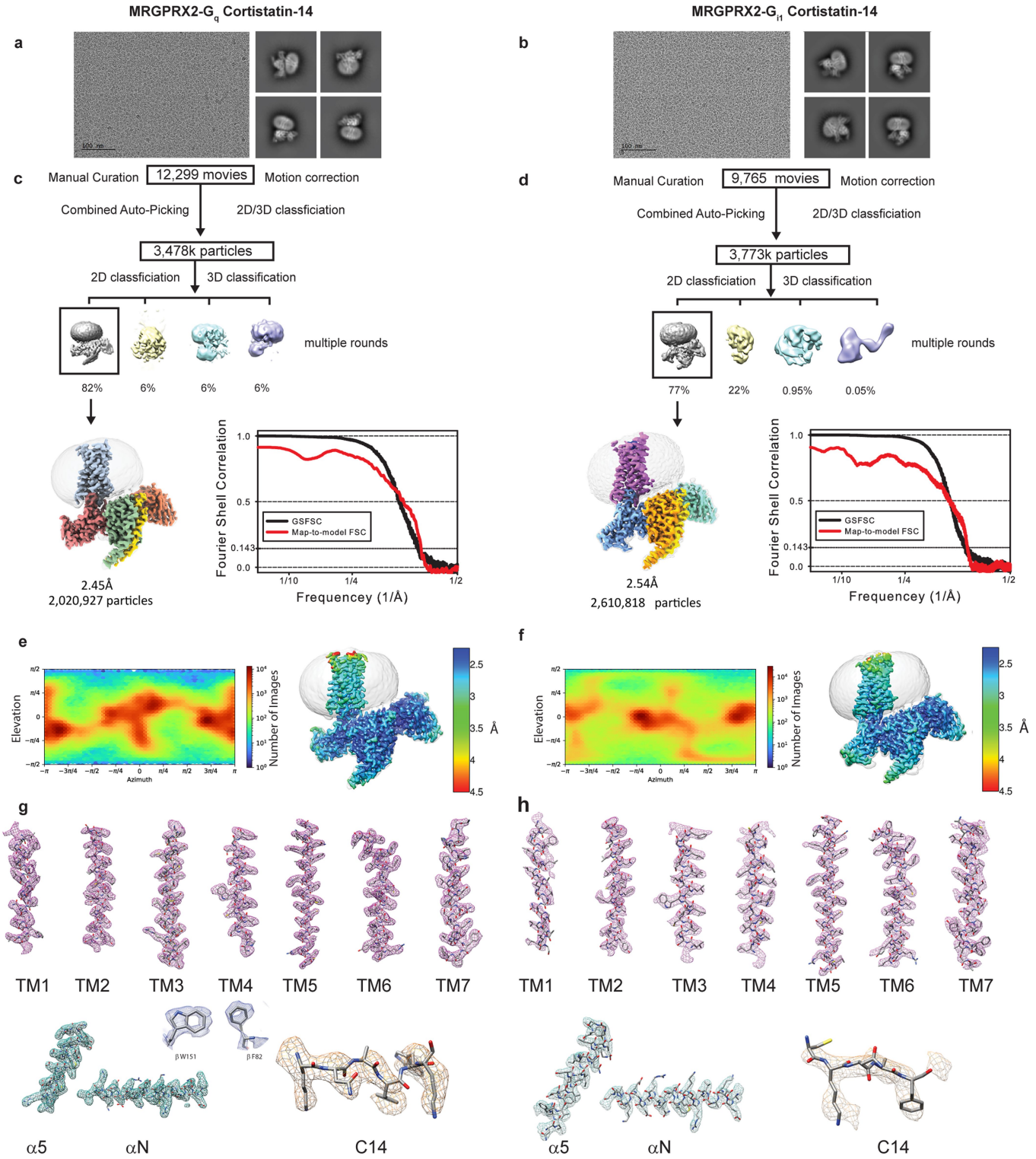

Extended Data Fig. 3 | CryoEM images and data-processing of MRGPRX2-G_q-Cortistatin-14 and MRGPRX2-G_{i1}-Cortistatin-14 complex. **a**, **b**, Representative motion corrected cryo-EM micrograph (scale bar, 100 nm) of MRGPRX2 G-protein cortistatin-14 (C14) particles imaged at a nominal 45k x magnification and representative two-dimensional class averages. The experiment was repeated three times with similar result. The exact number of movies and particles used for each complex are shown in the flow chart. **c**, **d**, Flow chart of cryo-EM data processing. GSFSC plot of auto-masked final map (black) and map-to-model real-space cross correlation (red) as calculated form phenix.mtriage. **e**, **f**, Viewing direction distribution and local resolution estimation heat maps. **g**, **h**, Local cryo-EM density maps of TM1-7, Cortistatin-14 ligand, α5 and α N helix of respective G-protein. Also shown inset are residues W151 and F82 of the b-subunit (blue).

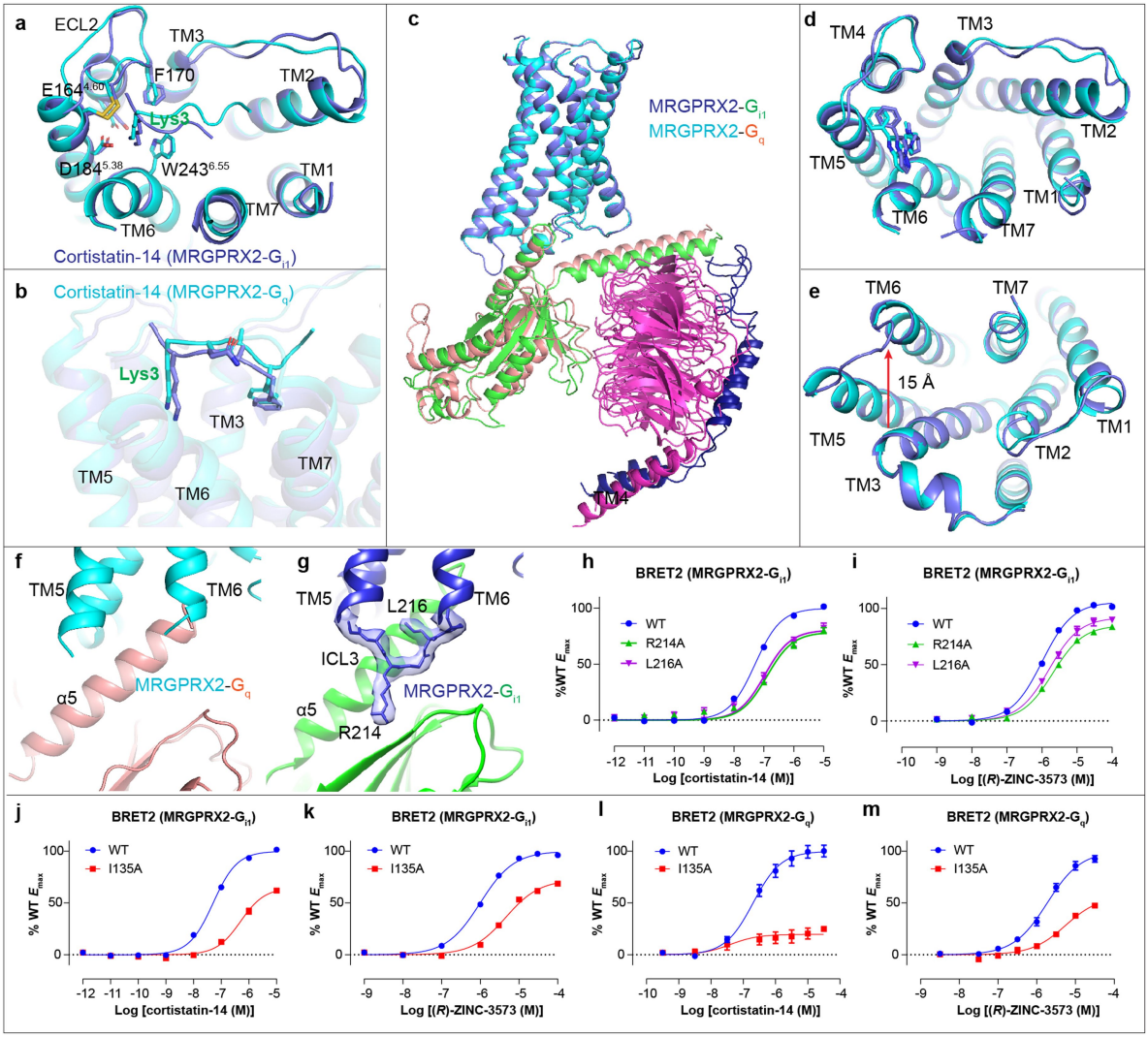

Extended Data Fig. 4 | Structural comparison of G_q- and G_{i1}-coupled MRGPRX2 complex. a, **b**, Structural comparison of the MRGPRX2-G_{i1}-cortistatin-14 complex (blue) with MRGPRX2-G_q-cortistatin-14 complex (cyan). Top view for the key interactions in sub-pocket 1 (**a**). Side view to show the overall conformational of cortistatin-14 (**b**). **c**–**e**, structural comparison of MRGPRX2-G_{i1}-(*R*)-ZINC-3573 complex with MRGPRX2-G_q-(*R*)-ZINC-3573 complex. G_{i1} and G_q are shown in green and salmon, respectively. G_{i1}-coupled MRGPRX2 and G_q-coupled MRGPRX2 are shown in blue and cyan, respectively. Side view of the whole complex (**c**), top view (**d**) and bottom view (**e**) of MRGPRX2. **f**, ICL3 of G_q is not clearly resolved in the G_q-coupled MRGPRX2 complex. **g**, Close-up view of the ICL3 in the G_{i1}-coupled MRGPRX2 structure with surrounding EM map at a threshold of 0.14. **h**, **i**, MRGPRX2 ICL3 mutations $R214^{ICL3}A$ and $L216^{ICL3}A$ impair cortistatin-14 (**h**) and (*R*)-ZINC-3573 (**i**) stimulated G_{i1} activation. Data represent mean ± s.e.m. of $n = 3$ biological replicates. **j**, **k**, BRET2 G_{i1} assays reveal that $I135^{ICL2}A$ mutation of MRGPRX2 attenuates cortistatin-14 (**j**) and (*R*)-ZINC-3573 (**k**) stimulated G_{i1} activation. Data represent mean ± s.e.m. of $n = 3$ biological replicates. **l**–**m**, BRET2 G_q assays reveal that $I135^{ICL2}A$ mutation of MRGPRX2 greatly reduced cortistatin-14 (**l**) and (*R*)-ZINC-3573 (**m**) stimulated G_q activation. Data represent mean ± s.e.m. of $n = 3$ biological replicates.

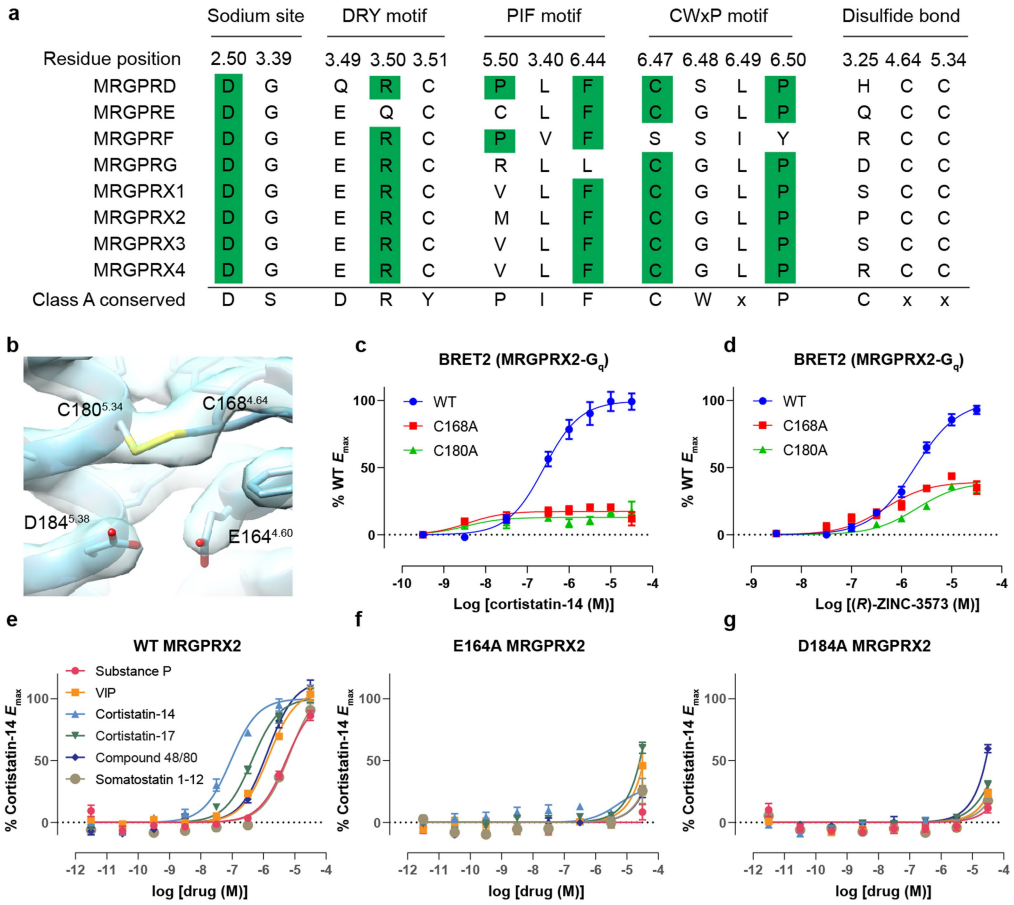

Extended Data Fig. 5 | Non-conserved motifs in Mas-related GPCRs and the critical role of acidic residues E164$^{4.60}$ and D184$^{5.38}$ in MRGPRX2 activation. **a**, Sequence alignment of the key residues in sodium site, DRY motif, PIF motif and CWxP motif, as well as residues involved in disulfide bond formation in Mas-related GPCRs. Class A conserved residues are highlighted in green. **b**, cryoEM map of the TM4-TM5 disulfide bond in MRGPRX2-G_q-(*R*)-ZINC-3573 complex. **c**, **d**, Break of the TM4-TM5 disulfide bond by C168$^{4.64}$A and C180$^{5.34}$A mutations abolishes the cortistatin-14 stimulated G_q activation (**c**) and reduces the E_{max} of (*R*)-ZINC-3573 stimulated G_q activation by 60% (**d**). Data represent mean ± s.e.m. of $n = 3$ biological replicates. **e**–**g**, Compared with WT (**e**), E164$^{4.60}$A (**f**) and D184$^{5.38}$A (**g**) totally abolish the peptide stimulated G_q activation of MRGPRX2. Data represent mean ± s.e.m. of $n = 3$ biological replicates.

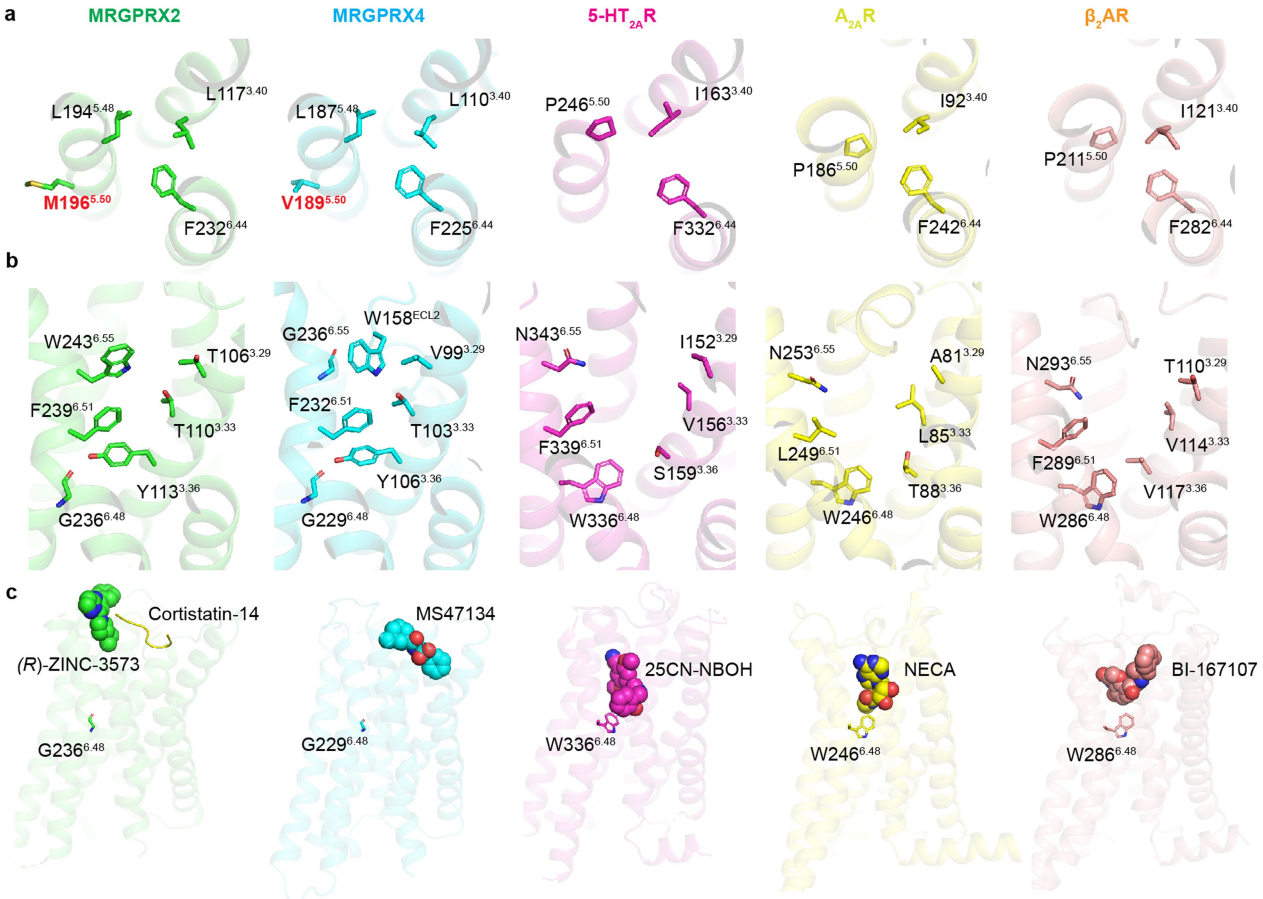

Extended Data Fig. 6 | Unique structural features of MRGPRX2 and MRGPRX4. a, MRGPRX2 and MRGPRX4 have a unique structural arrangement at the PIF motif compared with the G protein coupled active structures of 5-HT_{2A}R (PDB ID 6WHA), A_{2A}R (PDB ID 5G53) and β_2AR (PDB ID 3SN6). Residue 5.50 shifts away from the TM3-TM6 interface and does not engage $L^{3.40}$ and $F^{6.44}$ in MRGPRX2 and MRGPRX4. **b**, With $G^{6.48}$, TM6 of both MRGPRX2 and MRGPRX4 packs closer to TM3 compared with the G protein coupled active structures of 5-HT_{2A}R (PDB ID 6WHA), A_{2A}R (PDB ID 5G53) and β_2AR (PDB ID 3SN6), leading to an occluded canonical agonist binding pocket. **c**, (*R*)-ZINC-3573, cortistatin-14 and MS47134 bind to MRGPRX2 and MRGPRX4 at a position that is far away from residue 6.48, respectively. Cortistatin-14 is shown as cartoon. Small molecule compounds of receptors are shown as spheres.

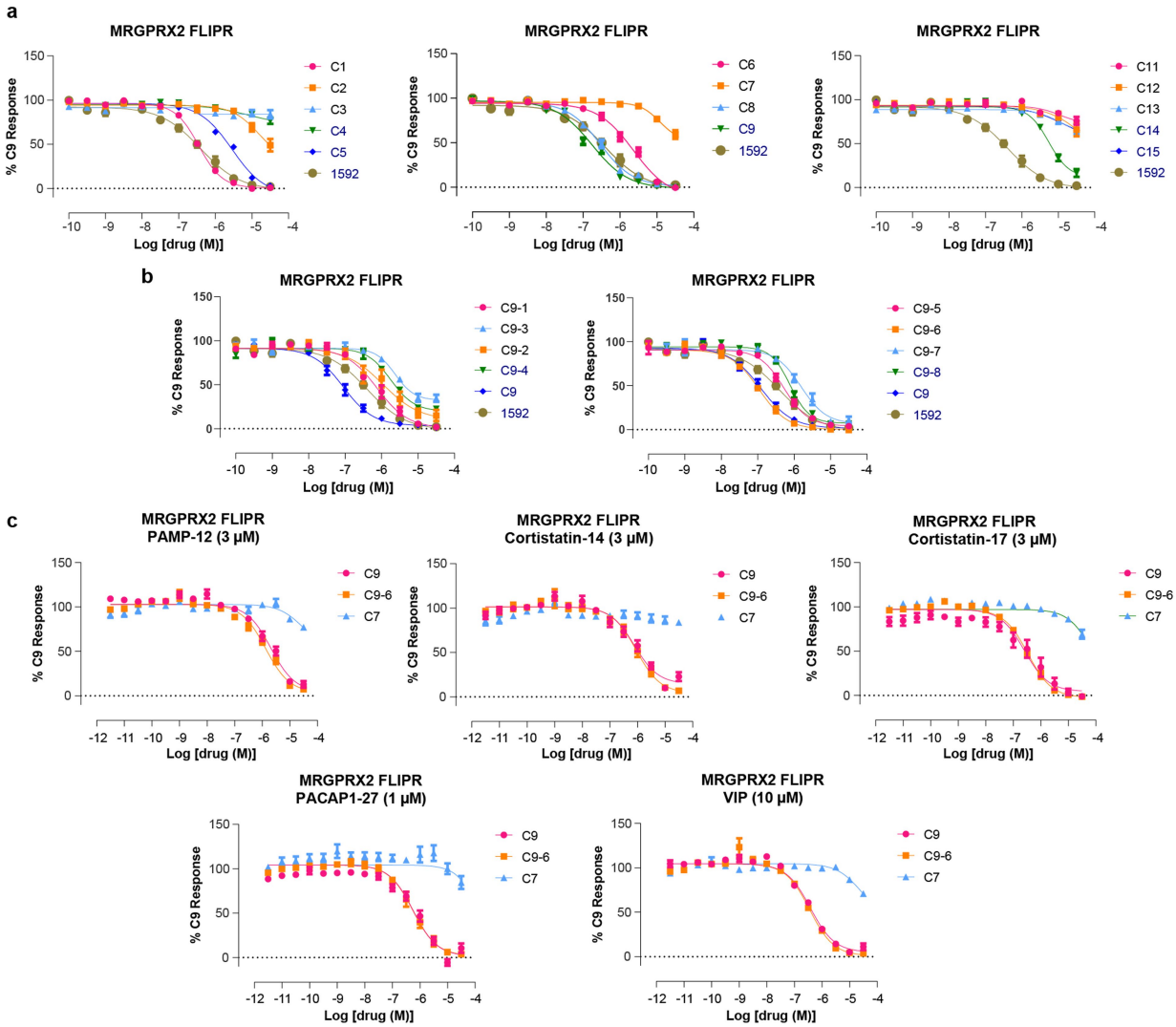

Extended Data Fig. 7 | Analog screening and functional characterization of MRGPRX2 antagonists. a, **b**, Dose-response curves of initial 14 analogs of '1592 (**a**) and 8 analogs of C9 (**b**) in the presence of EC_{80} concentration of (*R*)-ZINC-3573 using MRGPRX2 FLIPR Ca^{2+} assay. Data represent mean ± s.e.m. of $n = 3$ biological replicates. **c**, Dose-response curves of two potent MRGPRX2 antagonists C9 and C9-6 and an inactive compound C7 in the presence of EC_{80} of each MRGPRX2 peptide using MRGPRX2 FLIPR Ca^{2+} assay. Data represent mean ± s.e.m. of $n = 3$ biological replicates.

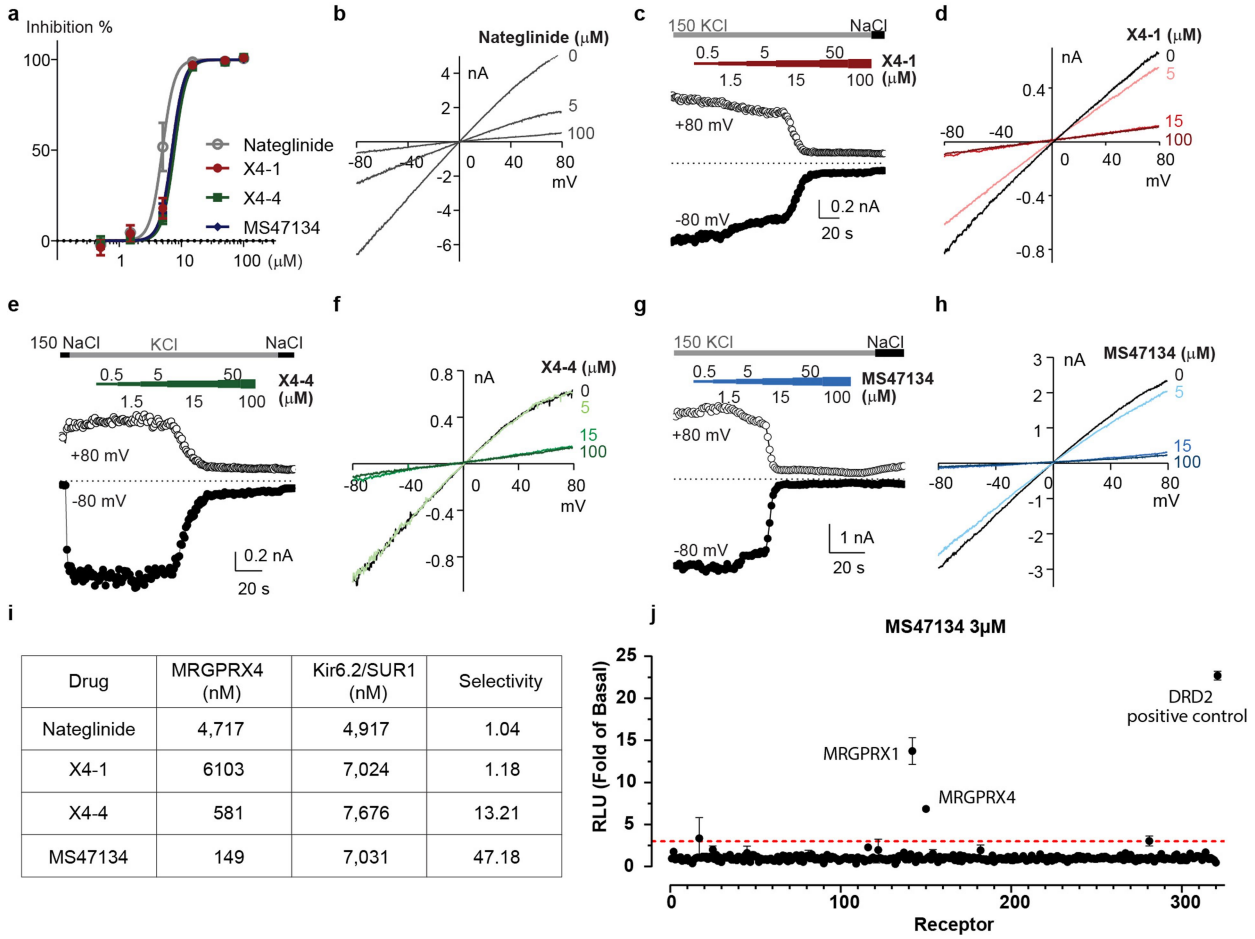

i

Drug	MRGPRX4 (nM)	Kir6.2/SUR1 (nM)	Selectivity
Nateglinide	4,717	4,917	1.04
X4-1	6103	7,024	1.18
X4-4	581	7,676	13.21
MS47134	149	7,031	47.18

Extended Data Fig. 8 | Functional characterization of optimized MRGPRX4 agonists. a, Dose-response curves of Kir6.2/SUR1 current inhibition by indicated chemicals. Data represent mean ± s.e.m. from *n*=4 biological replicates. **b**, **d**, **f**, **h**. Current-voltage relationships of whole-cell traces recorded in 150 mM KCl with the supplements of indicated chemicals of the labeled concentrations. **c**, **e**, **g**, Time courses showing the whole-cell-current responses to the indicated chemicals of the labeled concentrations. **i**, MRGPRX4 agonists X4-4 and MS47134 have a higher selectivity over Kir6.2/SUR1 channel compared with nateglinide. EC_{50} (nM) of each tested compound is shown. **j**, Screening of MS47134 across the GPCRome (at 320 receptors) using the PRESTO-Tango platform with 3 μM MS47134. Red dashed line indicated threefold of basal levels. Data represent mean ± s.e.m. of fold over basal for each receptor (*n*=4 technical replicates).

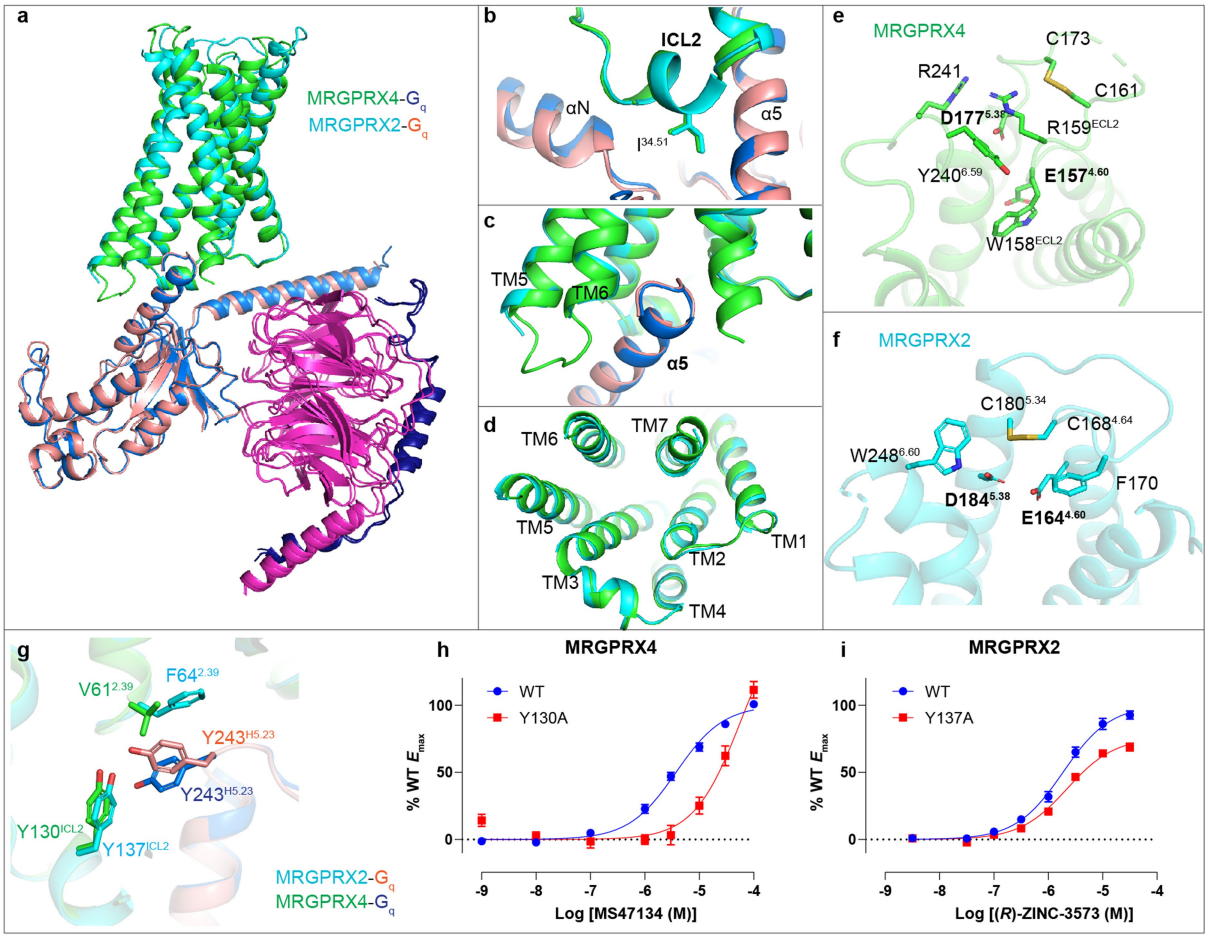

Extended Data Fig. 9 | Structural comparison of G_q-coupled MRGPRX2 and MRGPRX4. a–**d**, Structural comparison of the MRGPRX4-G_q-MS47134 complex with the MRGPRX2-G_q-(*R*)-ZINC-3573 complex. The receptor and G_q protein of MRGPRX4-G_q complex are colored by green and blue, respectively. The receptor and G_q protein of MRGPRX2-G_q complex are colored by cyan and salmon, respectively. Side view (**a**), Close-up view of αN-ICL2 interaction region (**b**), α5 helix region (**c**), and the cytoplasmic side of receptors (**d**). **e**, The acidic residues $E157^{4.60}$ and $D177^{5.38}$ of MRGPRX4 are shielded by the inserted ECL2. Side chain of D177 is not resolved but modeled here for a better visual interpretation. **f**, Residues $E164^{4.60}$ and $D184^{5.38}$ of MRGPRX2 extend to the cationic agonists accessible pocket. **g**, Due to the variance in residue 2.39, $Y243^{H5.23}$ of G_q adopts different side-chain conformations to interact with $Y130^{ICL2}$ of MRGPRX4 and $Y137^{ICL2}$ of MRGPRX2. **h**, **i**, BRET2 G_q assays for $Y130^{ICL2}$A of MRGPRX4 (**h**) and $Y137^{ICL2}$A of MRGPRX2 (**i**). Data represent mean ± s.e.m. of $n = 3$ biological replicates.

Extended Data Table 1 | Cryo-EM data collection, refinement and validation statistics

	MRGPRX2-G_q Cortistatin-14 (EMD-24896) (PDB 7S8L)	MRGPRX2-G_{i1} Cortistatin-14 (EMD-24897) (PDB 7S8M)	MRGPRX2-G_q (*R*)-ZINC-3573 (EMD-24898) (PDB 7S8N)	MRGPRX2-G_{i1} (*R*)-ZINC-3573 (EMD-24899) (PDB 7S8O)	MRGPRX4-G_q MS47134 (EMD-24900) (PDB 7S8P)
Data collection and processing					
Magnification	45,000	45,000	45,000	45,000	45,000
Voltage (kV)	200	200	200	200	200
Electron exposure (e–/Å^2)	50.7 & 47.9	42.2 & 46.1	50.6	48.8	48.8
Number of movies used	12,299	9,765	5,359	5,759	4,506
Defocus mean (SD) μm[1]	1.2 (0.5)	1.3 (1.1)	1.9 (0.5)	1.5 (0.8)	1.4 (0.4)
Pixel size (Å)	0.91	0.91	0.91	0.91	0.91
Symmetry imposed	C1	C1	C1	C1	C1
Initial particle images (no.)	3,478,202	3,733,419	1,878,853	2,629,570	3,170,704
Final particle images (no.)	2,029,927	2,610,818	318,836	705,283	599,186
Map resolution (Å)[2]	2.45	2.54	2.90	2.58	2.60
FSC threshold 0.143	0.143	0.143	0.143	0.143	0.143
Map resolution range (Å)	2.11-5.22	2.18-4.91	2.55-5.32	2.27-4.85	2.25-6.05
Refinement					
Initial model used (PDB code)	6WHA	6PT0	6WHA	6PT0	6WHA
Model resolution (Å)	2.74	2.83	3.13	2.86	2.87
FSC threshold	0.5	0.5	0.5	0.5	0.5
Map sharpening *B* factor (Å^2)	-89.8	-107.1	−106.5	-94	-88.6
Model composition					
Non-hydrogen atoms	8177	8346	8154	8331	8093
Protein residues	1096	1102	1090	1101	1089
Ligands	/	/	1	1	1
B factors (Å^2)					
Protein	48.64	52.94	63.61	50.48	120.78
Ligand	/	/	66.89	56.81	172.98
R.m.s. deviations					
Bond lengths (Å)	0.003	0.004	0.011	0.005	0.005
Bond angles (°)	0.550	0.583	0.879	0.698	0.725
Validation					
MolProbity score	1.27	1.64	1.55	1.50	1.49
Clashscore	2.51	6.45	4.10	3.12	3.12
Poor rotamers (%)	0.00	0.00	0.00	0.00	0.00
Ramachandran plot					
Favored (%)	96.46	95.93	94.86	94.18	94.21
Allowed (%)	3.54	4.07	5.14	5.82	5.79
Disallowed (%)	0.00	0.00	0.00	0.00	0.00

1 underfocus positive 2 Resolution estimates from cryoSPARC auto-corrected GSFSC

nature research

Corresponding author(s): Brian K. Shoichet, Jonathan F. Fay and Bryan L. Roth

Last updated by author(s): Nov 6, 2021

Reporting Summary

Nature Research wishes to improve the reproducibility of the work that we publish. This form provides structure for consistency and transparency in reporting. For further information on Nature Research policies, see our Editorial Policies and the Editorial Policy Checklist.

Statistics

For all statistical analyses, confirm that the following items are present in the figure legend, table legend, main text, or Methods section.

n/a	Confirmed	
☐	☒	The exact sample size (*n*) for each experimental group/condition, given as a discrete number and unit of measurement
☐	☒	A statement on whether measurements were taken from distinct samples or whether the same sample was measured repeatedly
☐	☒	The statistical test(s) used AND whether they are one- or two-sided *Only common tests should be described solely by name; describe more complex techniques in the Methods section.*
☒	☐	A description of all covariates tested
☐	☒	A description of any assumptions or corrections, such as tests of normality and adjustment for multiple comparisons
☐	☒	A full description of the statistical parameters including central tendency (e.g. means) or other basic estimates (e.g. regression coefficient) AND variation (e.g. standard deviation) or associated estimates of uncertainty (e.g. confidence intervals)
☐	☒	For null hypothesis testing, the test statistic (e.g. *F*, *t*, *r*) with confidence intervals, effect sizes, degrees of freedom and *P* value noted *Give P values as exact values whenever suitable.*
☒	☐	For Bayesian analysis, information on the choice of priors and Markov chain Monte Carlo settings
☒	☐	For hierarchical and complex designs, identification of the appropriate level for tests and full reporting of outcomes
☒	☐	Estimates of effect sizes (e.g. Cohen's *d*, Pearson's *r*), indicating how they were calculated

Our web collection on statistics for biologists contains articles on many of the points above.

Software and code

Policy information about availability of computer code

Data collection	SerialEM V3.8.2
Data analysis	cryoSPARC V3.1.0, Topaz 0.2.2, DeepEMhancer, Relion3.1, UCSF Chimera 1.15, cisTEM 1.0.0-beta, GemSpot, PyMol 2.4.1, Coot 0.9.5, MolProbity (built in phenix 1.18.2), Phenix 1.18.2, GraphPad Prism 9.0, ChemDraw 20.0.

For manuscripts utilizing custom algorithms or software that are central to the research but not yet described in published literature, software must be made available to editors and reviewers. We strongly encourage code deposition in a community repository (e.g. GitHub). See the Nature Research guidelines for submitting code & software for further information.

Data

Policy information about availability of data

All manuscripts must include a data availability statement. This statement should provide the following information, where applicable:

- Accession codes, unique identifiers, or web links for publicly available datasets
- A list of figures that have associated raw data
- A description of any restrictions on data availability

The coordinate and cryoEM map of MRGPRX2-Gq-cortistatin-14, MRGPRX2-Gi1-cortistatin-14, MRGPRX2-Gq-(R)-ZINC-3573, MRGPRX2-Gi1-(R)-ZINC-3573 and MRGPRX4-Gq-MS47134 have been deposited to PDB and EMDB with accession code 7S8L (EMD-24896), 7S8M (EMD-24897), 7S8N (EMD-24898), 7S8O (EMD-24899) and 7S8P (EMD-24900), respectively. The cryoEM micrographs of MRGPRX4-Gq-MS47134, MRGPRX2-Gq-cortistatin-14, MRGPRX2-Gq-(R)-ZINC-3573, MRGPRX2-Gi1-cortistatin-14 and MRGPRX2-Gi1-(R)-ZINC-3573 have been deposited to EMPIAR database with accession number of EMPIAR-10852, EMPIAR-10853, EMPIAR-10854, EMPIAR-10855 and EMPIAR-10856, respectively. PDB database (https://www.rcsb.org/) was used in this study to download the structures of 5-HT2AR-Gq (PDB ID 6WHA), A2AR-miniGs (PDB ID 5G53), β2AR-Gs (PDB ID 3SN6) and CB2-Gi complex (6PT0) for structural analysis.

Field-specific reporting

Please select the one below that is the best fit for your research. If you are not sure, read the appropriate sections before making your selection.

☒ Life sciences ☐ Behavioural & social sciences ☐ Ecological, evolutionary & environmental sciences

For a reference copy of the document with all sections, see nature.com/documents/nr-reporting-summary-flat.pdf

Life sciences study design

All studies must disclose on these points even when the disclosure is negative.

Sample size	No statistical methods used to predetermine sample size. For cryoEM studies, the number of micrographs is determined by the available microscope time. For FLIPR, BRET and ELISA assays, three biologically independent experiments (n=3) were performed. For LAD2 human mast activation, two biologically independent experiments (n=2) was performed in quadruplicate. For electrophysiology experiments, four biologically independent experiments (n=4) were performed. For the time-consuming and labor-intensive GPCRome assay for 320 GPCRs, one biologically independent experiment was performed with n=4 technical replicates. Only initial positive hits from GPCRome were then replicated in subsequent dose-response assay with three biologically independent experiments (n=3).
Data exclusions	No data were excluded.
Replication	For FLIPR, BRET and ELISA assays, three biologically independent experiments (n=3) were performed. For LAD2 human mast activation, two biologically independent experiments (n=2) was performed in quadruplicate. For the GPCRome assay, one biologically independent experiment was performed with n=4 technical replicates. For electrophysiology experiments, four biologically independent experiments (n=4) were performed. All attempts at replication were successful.
Randomization	For cryoEM study, meshes on the grids with good ice thickness were randomly selected for data collection. For the functional assays including FLIPR, BRET, ELISA, GPCRome and electrophysiology experiments, randomization is not relevant as no group allocations were performed.
Blinding	No blinding was performed in this study. For both cryoEM structure determination and functional studies, blinding is not necessary due to the nature of these experiments do not requires subject assessment of the data that may influence the validity of the results.

Reporting for specific materials, systems and methods

We require information from authors about some types of materials, experimental systems and methods used in many studies. Here, indicate whether each material, system or method listed is relevant to your study. If you are not sure if a list item applies to your research, read the appropriate section before selecting a response.

Materials & experimental systems

n/a	Involved in the study
☐	☒ Antibodies
☐	☒ Eukaryotic cell lines
☒	☐ Palaeontology and archaeology
☒	☐ Animals and other organisms
☒	☐ Human research participants
☒	☐ Clinical data
☒	☐ Dual use research of concern

Methods

n/a	Involved in the study
☒	☐ ChIP-seq
☒	☐ Flow cytometry
☒	☐ MRI-based neuroimaging

Antibodies

Antibodies used	gp64-PE antibody, anti-FLAG–horseradish peroxidase–conjugated antibody
Validation	gp64-PE (R-PHYCOERYTHRIN (R-PE)-conjugated mouse anti-baculovirus monoclonal antibody is from mouse clone AcV1 and used for baculovirus titration. Detailed information can be found at: https://expressionsystems.com/product/gp64-pe-antibody/ anti-FLAG–horseradish peroxidase–conjugated antibody is from mouse clone M2 and used for measuring protein expression on the surface of cells. Detailed information can be found at: https://www.sigmaaldrich.com/US/en/product/sigma/a8592

Eukaryotic cell lines

Policy information about cell lines

Cell line source(s)	HEK293T cells were purchased from the American Type Culture Collection (ATCC, ATCC CRL-11268). LAD2 human mast cell. H3K293 Cells.Tetracycline-inducible MRGPRX2 and MRGPRX4 were generated according to manufacturer's instructions from the FLP-IN/T-REX HEK-293 cells (Invitrogen, Cat#R78007) and were certified as HEK 293 cells. NK1R stably expressing CHO cell

	lines are derived from Dr. James E. Krause's lab. LAD2 cells were supplied by Dr. A.S Kirshenbaum at NIAID. HTLA cells were a gift from R. Axel (Columbia University)
Authentication	HEK293T cells were authenticated by the supplier (ATCC) using morphology and growth characteristics, and STR profiling. HEK293 cells were authenticated using morphologies and growth characteristics according to instructions on ThermoFisher website. LAD2 cells were authenticated by demonstrating degranulation by crosslinking of FceR1 and expression of CD34, CD63 and CD117. HTLA cells (a HEK293 cell line stably expressing a tTA-dependent luciferase reporter and a β-arrestin2-TEV fusion gene) were a gift from R. Axel and was authenticated by morphology, growth characteristics and the successful tango assay which demonstrates that both tTA-dependent luciferase reporter and a β-arrestin2-TEV fusion gene are presented in the cells.
Mycoplasma contamination	HEK293T cells have been tested and shown to be free from mycoplasma (Hoechst DNA strain and Direct Culture methods employed). HEK293 cells, NK1R stable cells, HTLA cells and LAD2 cells were not in particular tested for mycoplasma contamination
Commonly misidentified lines (See ICLAC register)	None